# Ultimate Bending Capacity of Spiral-Welded Steel Tubes - Part I: Experiments

# Ultimate Bending Capacity of Spiral-Welded Steel Tubes – Part I: Experiments

Sjors H.J. van Es[1], Arnold M. Gresnigt

*Delft University of Technology, Delft, The Netherlands*

Daniel Vasilikis, Spyros A. Karamanos

*University of Thessaly, Volos, Greece*

## ABSTRACT

The present investigation refers to the bending capacity of spiral-welded steel tubes. The first part of this investigation presents the results of a full-scale experimental program, aiming to investigate the structural behavior of large-diameter spiral-welded steel tubes under bending. A companion paper (Part II) is also published which further studies the behavior of these elements numerically, using finite element simulations.

The testing program presented in Part I consists of thirteen 42-inch-diameter spiral-welded steel tubes with D/t ranging between 65 and 120. Some of the tubular specimens contain girth welds and coil connection welds, which are shown to penalize the ultimate bending capacity of the tubes. Extensive measurements of initial imperfections and material properties are performed for each tubular specimen. The material properties of the specimens are investigated through both uniaxial tensile and compression coupon tests. A series of large-scale four-point bending tests is performed to determine the structural behavior of the tubes, resulting in local buckling failure of the tubes under consideration.

The bending behavior of the thirteen specimens is documented extensively. The study offers information with regard to the ultimate bending resistance of the specimens. In addition, the full moment-curvature equilibrium path is presented, supplemented by measurements on the development of cross sectional ovalisation and tube wall wrinkling during the bending tests.

## 1 INTRODUCTION

An economical and efficient method to manufacture relatively thin-walled large-diameter steel tubes is offered by the spiral-welded (or helical-welded) manufacturing process (HSAW). This process consists of spiral welding of a steel plate from a hot-rolled steel coil, as shown schematically in Figure 1. Common spiral-welded tube diameters range from about 500 to 3000 mm, with wall thicknesses between 9 and 25 mm. The manufacturing process is continuous; a steel coil that runs out is connected to a new coil by means of a butt weld without interruption of the spiral-welding process. This weld,

[1] Corresponding author, email S.H.J.vanEs@TUDelft.nl

running perpendicular between two spiral welds is denoted in this study as a coil connection weld (CCW). In addition to these coil connection welds, girth welds are also present in elements used in practice. These girth welds may be executed in the controlled environment of the production plant, but for the connection of adjacent tube segments, girth welds can also be executed on-site.

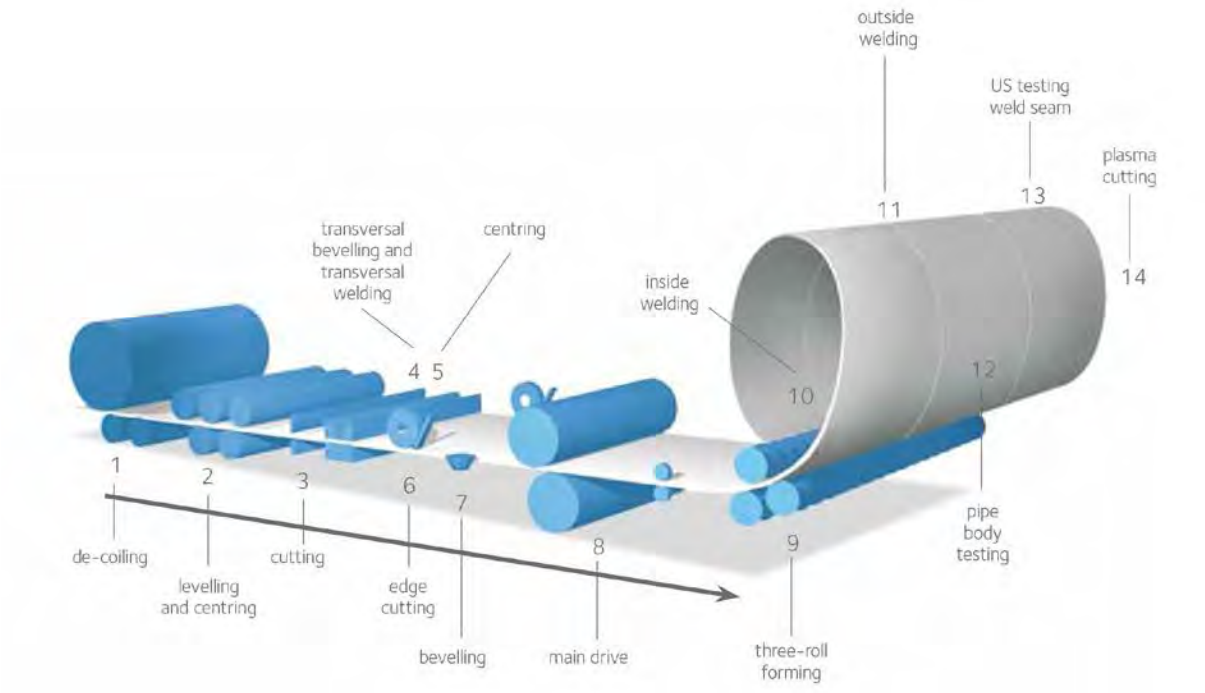


**Figure 1:** Schematical overview of HSAW production process [1].

Large-diameter spiral-welded tubes are employed in onshore hydrocarbon and water pipeline applications. The diameter of hydrocarbon pipes can range from 700 mm up to about 1500 mm, with $D/t$ ratios between 40 and 100. In addition to hydrocarbon pipelines, large-diameter steel pipelines and penstocks for water transmission are very often made of spiral-welded tubes. The diameter of large-diameter steel tubes for water transmission typically ranges from 900 to 2000 mm, with rather high diameter-to-thickness ratios; $D/t$ ranges can range up to 240. Spiral-welded tubes are also used in structural applications, for example for tubular piling, towers, masts and other large tubular structures. An important structural application is the use of large-diameter steel tubes in combined walls as primary structural elements that resist horizontal loads from soil and water pressure. Those combined walls, often referred to as "combiwalls", consist of a series of large diameter tubes connected by infill sheeting (see Figure 2). For their connection, standard sheet piling slots are welded to the tube. Steel tubes used in combined walls are generally manufactured with the spiral welding process, with a diameter range up to 3000 mm, thickness up to 25 mm, specified minimum yield strength between 350 MPa and 480 MPa, and length up to 50 meters, whereas typical values of the corresponding diameter-to-thickness ratio range from 65 to 120. An advantage of using the continuous spiral-welding manufacturing process for tubes in this application is the capability of producing tubes of significant length, thereby minimizing the number of girth welds in the structure.

**Figure 2**: Example of a combined wall system under construction [2]

The present work is motivated primarily by the need of determining the structural capacity of large-diameter spiral-welded tubes, employed in combiwall applications [3], [4]. In this application, the main loading condition is bending of the tube, and the corresponding dominant failure mode is local buckling of the tube wall. The linear and nonlinear bending behavior of spiral-welded tubes is also important for the response and safe design of large-diameter pipelines, subjected to severe ground-induced deformations in geo-hazard areas. In those areas, the pipeline is subjected to significant bending loading due to fault movement, liquefaction-induced lateral spreading and subsidence, as well as landslide action which may threaten its structural integrity.

Longitudinal bending deformation of a tubular member induces ovalisation of the tube cross-section, a special feature of tube bending, also known as the "Brazier effect" [5]. Ovalisation reduces the tube bending stiffness because of flattening, increases the local radius of the tube cross-section at the maximum compression location, and introduces a biaxial stress state, because of ring bending, leading to early yielding of the tube. Upon increasing bending deformation, structural instability of the compressed tube wall occurs, in the form of a localized wavy pattern, referred to as "local buckle", "wrinkle" or "kink". The formation of a local buckle is associated with a bending moment drop in the moment-curvature equilibrium path of the tubular member; this means structural failure of the tubular member. Based on previous experimental observations, thin-walled tubes with $D/t$ values equal or above 100 subjected to bending develop wrinkles quite rapidly, leading to sudden collapse. On the other hand, in bent tubes with $D/t$ values equal to about 60 or 70, the development of wrinkles is more gradual.

The pure bending response of metal tubes has been investigated experimentally numerous times in the last decades. Early experimental work was conducted by Moore and Clark [6] on specimens machined from aluminum-alloy rolled rod with $D/t$ ratios ranging from 2 to 150. Their scaled experiments include bending, compression and torsion testing of which the former two are of interest for the current research. Specimens with $D/t$ ratios larger than 15 were found to be prone to instability,

either due to progressive ovalisation or the formation of a local buckle. The influence of axial tension on local buckling was found to be positive by Wilhoit and Merwin [7] in similar scaled bending experiments. A large number of small scale bending tests has been performed by Johns et al. [8]. The use of small scale experiments allowed the application of combined load of external pressure and bending. By validating the large number of scaled tests with a limited number of full scale four-point bending tests, understanding of the local buckling mechanism was further increased. More bending tests on small scale specimens were performed by Tugcu and Schroeder [9], whose research includes mainly tests on tube branches besides a few tests on plain tube, and Reddy [10], who tested tubing with $D/t$ ratios up till 80 made of steel and aluminum. The latter investigation also includes the measurement of longitudinal profiles of the tubing at the onset of local buckling. Testing on slender tubes ($D/t$=81-102) of intermediate scale was performed by Van Douwen et al. [11], focusing on the application of pipelines in settlement areas. Small-scale specimens have been tested by Kyriakides and Shaw [12] and Kyriakides and Ju [13]. In these two publications combined, more than twenty tests on steel and aluminum specimens under monotonic or cyclic bending are reported.

Early large scale testing was performed by Jirsa et al. [14]. The work features six four-point bending tests on tubes up to 20 inch, two of which are concrete-coated. The moment-curvature diagrams that result from the tests were simulated by an analysis method published earlier by Ades [15], which allows an cross-sectional analysis of the bending behavior of the specimens, including the Brazier effect, but cannot capture the formation of a local buckle. Further large scale testing was performed by Sherman [16]. The testing program includes tubes with $D/t$ ratios between 18 and 102 with various loading conditions leading to a combination of bending moment and shear force at the critical cross sections of the specimens. More recently, more than fifty bending tests on plain and girth welded tubes were performed at the University of Alberta, which are documented in Dorey et al. [17], Delcol et al. [18], Dorey et al. [19], Mohareb et al. [20] and Yoosef-Godsi et al. [21]. The tests were performed on specimens with $D/t$ ratios between 48 and 92. The results present a negative influence of the presence of a girth weld in the critical cross section.

One of the first investigations into the effect of the manufacturing technique of the tubes on their bending behavior was performed by Bouwkamp [22], who performed bending tests on longitudinal welded and seamless tubes. In another work by the same author [23], experimental investigations on the local buckling behavior of large diameter tubes (48 inch) have been reported. The work by Van Foeken and Gresnigt [24], [25] has further studied the influence of the manufacturing method of a tube on its local buckling behavior, by comparing the collapse and bending behavior of UOE manufactured tube with seamless tubes.

Experimental investigation on the bending behavior of spiral-welded tubes is relatively rare. The work by Zimmerman et al. [26] includes bending experiments on four spiral-welded tubes with $D/t$ ratios between 48 and 82. Two of these experiments included internal pressure resulting in a hoop stress of 80% of the specified minimum yield strength. A direct experimental comparison with other manufacturing techniques has not been conducted, but a comparison is made with experimental data from literature. The study concludes that the spiral weld seam may not be detrimental to tube performance and that spiral-welded line pipe performs as good as longitudinal welded linepipe in terms of local buckling behavior. Further experimental testing on spiral-welded tubes was performed by

Salzgitter Mannesmann, reported by Zimmermann et al. [27]. In that research, four-point bending tests were performed on four spiral-welded tubes. During the bending tests in this investigation, two of the specimens were pressurized up to a level leading to a hoop stress of 66% of the specified minimum yield strength. In comparison with common design standards, the performance of the specimens is deemed to be satisfactory. Neither the work in [26] or the work in [27] includes a study into the influence of a girth weld or coil connection weld on the local buckling behavior. Further investigation of the behavior of spiral-welded tubes including a girth weld in the critical bending zone is announced in [27], but has not yet been published. Eight bending tests on spiral-welded tubes have been performed by Reinke et al. [28] as part of the same European research project the present investigation is part of. The research concludes that the experiments show that the spiral welded tubes performed well and that the influence of spiral-welding on the bearing behavior of the specimens is negligible.

The present investigation is part of a large research project with acronym COMBITUBE, funded by the European Commission in the framework of the RFCS program [29]. The investigation is aimed at examining the bending behavior of large-diameter steel tubes, focusing on the determination of their ultimate bending moment capacity and the corresponding buckling curvature, taking into account the effects of the spiral-welding manufacturing process. Furthermore, typical features of spiral-welded tubulars used in structural applications, such as a girth weld or a coil connection weld, are included. The current research includes a thorough experimental investigation on 42-inch-diameter steel tubes with extensive measurements of the initial geometry of the tubes. Aside from the large-scale experimental testing, numerical simulations with finite elements are also included in the investigation. In this paper, denoted as Part I, the experimental testing and corresponding results are presented in detail. The companion paper by Vasilikis et al. [30], referred to as Part II, reports the numerical simulation of the experimental procedure and an extensive parametric numerical study. The pair of papers are aimed at providing a comprehensive overview of the bending behavior of large-diameter spiral-welded tubes. Part I starts with the discussion of the manufacturing technique in section 2, whereas the presentation of the 42-inch-diameter tubular specimens and the experimental setup are offered in section 3. Measurements of initial imperfections and extensive material testing are presented in section 4. Section 5 describes the experimental results from the full-scale tests. Finally, conclusions are stated in section 6.

## 2 BRIEF DESCRIPTION OF THE SPIRAL-WELDED MANUFACTURING METHOD

The spiral-welding manufacturing technique is an economic solution for producing large-diameter tubes with a relatively high slenderness; i.e. with relatively small wall thickness. Commonly available diameters range from about 500 mm up to 3000 mm with wall thicknesses ranging from about 9 mm to 25 mm. The length of the produced tubulars may range from 8 m to about 50 m. Due to the continuous production, long lengths can be manufactured. The main limits on length are the available room in the plant and transportation capacity.

During manufacturing, the plate material is de-coiled, straightened and beveled at the edges. Then, the spiral is formed through cold deformation of the plate, usually via a three-roll bending system. The tube is continuously welded from two sides (inside and outside), resulting in an X-weld for the spiral

weld. Quality control takes place continuously in the form of ultrasonic testing of the weld seam, monitoring of the diameter of the product and monitoring the welding process parameters.

In comparison with manufacturing methods of longitudinal welded tubes, the spiral-welding manufacturing technique results in some interesting features of the produced tube. Firstly, the rolling direction of the parent coil material does not correspond with the main loading direction of the end product, since the original coil material is processed into a tube product at a certain angle, depending on coil width and desired tube diameter. Secondly, the cold forming process of a flat plate into a spiral tube results in a complex residual stress state. Finally, the end product features welds in various orientations (see Figure 3). Most obvious is the spiral weld, which joins the helically-formed coil. A second type of weld arises when two coil ends are connected by a butt weld in the continuous manufacturing process. This results in a butt weld running perpendicular between two spiral welds, denoted as a coil connection weld (CCW). Tubes with coil connection welds are generally not used in pipeline applications, but they can be present in tubes employed in structural applications. In case of connection between two tube elements, a girth weld (GW) is present. This weld can be executed at the manufacturing plant, but also on site.

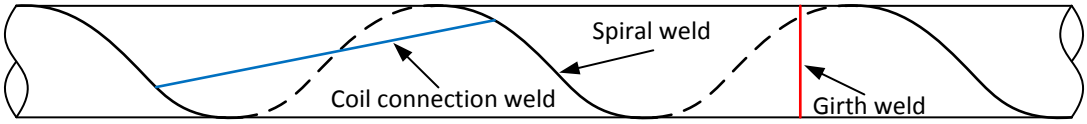


**Figure 3**: Schematic representation of a spiral-welded tube with a spiral weld, girth weld and coil connection weld.

## 3 EXPERIMENTAL SET-UP AND TUBULAR SPECIMENS

### 3.1 Outline of testing program and specimens

To investigate the local buckling behavior of spiral-welded tubes, a large-scale experimental program has been performed. The program features investigation of the initial geometry of the tubes, extensive material testing and four-point bending tests.

The program consists of thirteen 42-inch-diameter spiral-welded steel tubes. All specimens have a specified outer diameter of 1067 mm, with $D/t$ ratios varying from 65 to 120, a length of 16500 mm, and steel grades varying from X52 to X70. The investigation is not restricted to plain tubes with only a spiral weld, but also includes additional welds in the specimens such as girth welds and coil connection welds. Should such welds be present in a specimen, the specimen is divided by that weld into two or more sections, with each section having its own material and geometrical properties. These sections are referred to as ‘specimen parts’ and are identified by adding the indicators ‘left’, ‘middle’ and ‘right’ to the specimen identification.

An overview of the experimental program is depicted in Table 1. Considering the geometry of the four point bending setup, all investigations are focused at the central 8 meters of the specimen, the segment with constant bending moment during the bending test, as described in paragraph 3.3.

| Specimen I.D. | *D* [mm] | *t* [mm] | *D/t* | Type | Grade |
|---|---|---|---|---|---|
| T1 | 1066 | 16.4 | 65.1 | Plain | X70 |
| T2 | 1067 | 9.0 | 118 | Plain | X60 |
| T3 | 1069 | 9.0 | 118 | GW | X60 |
| T4 | 1065 | 9.2 | 116 | Plain | X60 |
| T5 | 1070 | 9.0 | 118 | Plain | X60 |
| T6 | 1066 | 16.3 | 65.3 | CCW | X70 |
| T7 | 1068 | 16.3 | 65.4 | GW & CCW | X70 |
| T8 | 1068 | 9.1 | 117 | Plain | X60 |
| T9 | 1069 | 16.3 | 65.4 | Plain | X70 |
| T10 | 1070 | 13.1 | 81.6 | GW & CCW | X52/X60* |
| T11 | 1068 | 12.9 | 83.0 | Plain | X52/X60* |
| T12 | 1069 | 9.1 | 117 | GW & CCW | X60 |
| T13 | 1070 | 9.2 | 117 | GW | X60 |

**Grade unknown at time of acquirement; estimate based on hardness measurements.*

**Table 1**: Overview of testing program. Dimensions averaged over specimen length.

On the basis of the results of the material tensile tests, measured wall thickness and initial imperfections and visual observation, some specimens appear to be very similar (e.g., all specimens with a wall thickness of about 9 mm). Furthermore, they have been acquired from the same provider at the same time. It is assumed that these specimens originate from the same manufacturer, possibly even from the same production batch.

### 3.2 Outline of material testing and initial geometry measurements

Correct interpretation of the test results requires information on the materials mechanical behavior. Furthermore, this can provide insight into the influences of cold forming during the production process and enable reliable modelling of the experiments in the companion paper which reports extensive finite element calculations.

For each specimen, tensile tests have been performed in the longitudinal direction of the tube axis and in the circumferential (hoop) direction from both the inside and outside of the tube wall. These specimens have been machined from the tube wall, so that flattening of the tensile coupon has not been necessary. In addition, from several specimens, full thickness specimens have been extracted, oriented in both longitudinal and hoop direction. Additional full thickness specimens have been taken in the directions axial and perpendicular with respect to the original coil. Tensile testing of small specimens extracted from the spiral welds has also been conducted.

Compression material tests have been performed on several tubes to examine whether the tension and compression behavior of the material is similar. To perform compression tests, small cylinders have been machined from the tube wall and compressed while being supported against rotation on either side. An overview of the compressive test setup is presented in Figure 4. The main focus of the

compression tests is to identify to what extend the cold forming of the plate material leads to asymmetry in the tension/compression behavior of the material.

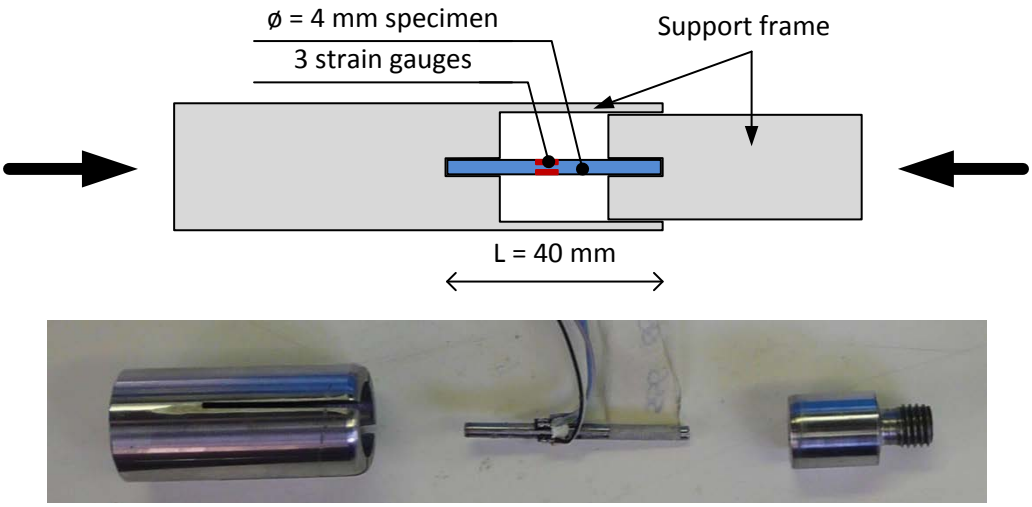


**Figure 4**: Schematic overview and photo of the compression test setup with the specimen, strain gauges and support.

The initial geometry of all specimens is documented in detail. First, the outer profile of the tube has been scanned using a laser trolley driving on rails below the specimen. An overview of the test setup is depicted in Figure 5. The tube is placed on two roller supports, enabling the operator to rotate it around its longitudinal axis. In this way, scans of the surface of the tube at various orientations are obtained. The first specimens have been scanned in eight orientations (every 45º), for later specimens the interval has been decreased to 22.5º. The "raw measurements" have been corrected to account for the sag of the tube under self-weight, non-levelness of the supports and any imperfections in the driving rails of the trolley. The latter correction has been performed by scanning a perfect fluid surface with the trolley, which is used as reference measurement.

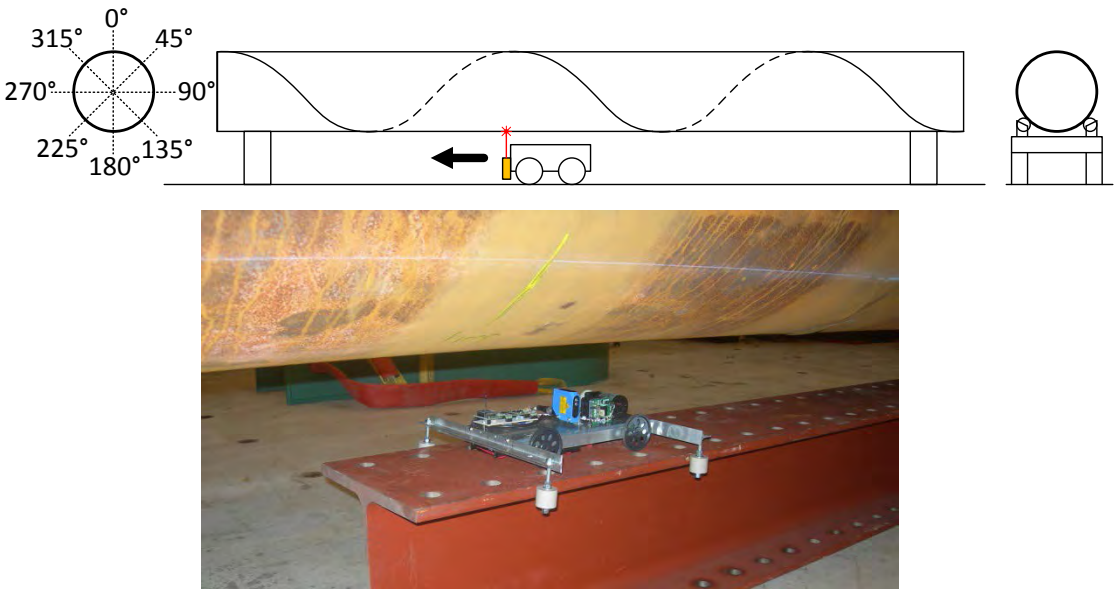


**Figure 5**: Schematic overview and photo of laser measurements of geometrical imperfections.

Furthermore, the tube diameter and wall thickness have been measured at several locations. More specifically, the thickness has been measured using an ultrasonic thickness measurement device at eight locations around the circumference and in five cross sections along the specimen center length. In addition, the thickness variation of the original coiled plate is investigated by a series of wall thickness measurements along a line perpendicular to the spiral welds. The tube diameter has been measured using a bracket fitted with laser distance sensors. By rotating the tube along its length axis, similar to the procedure followed during the profile scanning, diameter measurements at four different orientations have been obtained at five locations along the specimen center length.

### 3.3 Four-point bending set-up

To determine the maximum bending capacity of the tubes, the specimens are loaded in four-point bending until local buckling occurs. Considering the large diameter of the tubes, the forces involved in the test setup are of significant scale. The test setup has been designed to deliver a maximum of 3500 kN at each end of the specimen with a stroke of 350 mm. Considering these requirements and the limited availability of high capacity hydraulic actuators, different actuators have been used on each side of the test setup. Despite this difference, the loading on the specimen itself is symmetric. An overview of the test setup is shown in Figure 6.

To minimize the influence of the introduction of the loads into the specimen on the local buckling failure, loads are applied trough thin, flexible straps. Furthermore, at the middle support, the load is spread over two straps at each support, to further reduce any local effects due to the load introduction.

The bending tests are all performed in a displacement-controlled scheme. The displacements of the specimen ends are increased in small steps, after which a set of laser measurements is performed. After the formation of a local buckle, the loading is continued until the end of the actuators stroke is reached

or until a stage where further formation of the local buckle would cause damage to measurement equipment.

During the test, the specimen is oriented such that the intrados coincides with one of the scanned geometry profiles. Based on the initial geometry measurements presented in section 4.3, the most detrimental orientation of the tube has been chosen for testing (see section 4.3).

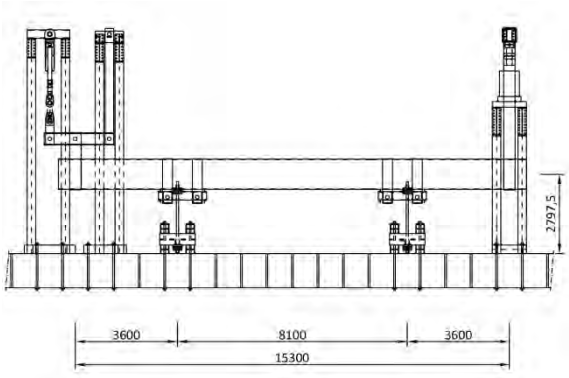


(a) Sketch of test set-up

(b) Overview photo of test set-up after formation of a local buckle

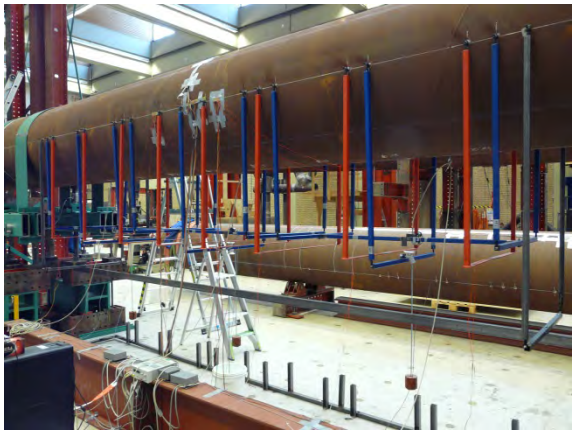

(c) Brackets for measurement of ovalisation and curvature

(d) Local buckle in specimen T11 ($D/t$=82.8)

**Figure 6**: Overview of four-point bending test setup

### *3.3.1 Continuous measurements*

During the test, a wide array of continuous measurements is performed. Naturally, the applied force and displacements at all four load application points are monitored. In addition to that, strains at the intrados and extrados of the bent specimen, horizontal ovalisation at eight locations and curvatures are measured. Curvature is measured using curvature brackets (see Figure 6c and Figure 7a). For each curvature measurement, three brackets are attached to the neutral axis of the specimen, of which the

outer two are coupled. The distance δ between the middle bracket and the coupler bar is used to calculate the bending curvature using a simple interpolation function: $\kappa=8\delta/L^2$, where $L$ is the distance between the two outer brackets.

Three brackets ($\kappa_1$, $\kappa_2$ and $\kappa_3$) are used to measure the curvature over a length of 1500 mm, which is roughly 1,4 times the specimen's diameter. One additional larger curvature measurement ($\kappa_{avg;b}$) is used to calculate the average curvature over a much larger length within the constant bending moment part of the bent tube. In addition to these measurements, the average curvature is also calculated from the measured displacements at the four load application points of the tube ($\kappa_{avg;U}$). The rotation of the mid-supports is calculated from these displacements and an elasto-plastic bending analysis of the two outer "loading arms" of the specimen. The bending curvature can then easily be determined from these rotations, assuming a constant curvature over the middle part of the tube.

The horizontal ovalisation of the tubes is measured by attaching brackets with flexible horizontal strips to the neutral line of the specimens. By measuring the strain in the bending horizontal strips with strain gauges, the horizontal ovalisation is determined (see Figure 7b).

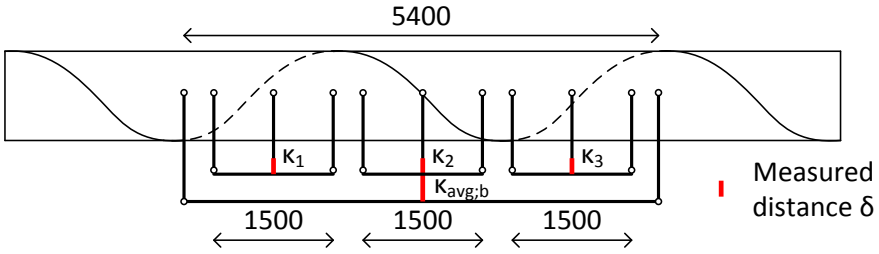


(a) Curvature measurements of the tubes.

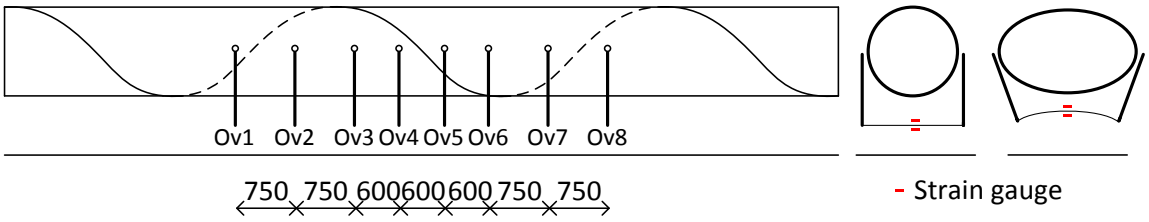


(b) Ovalisation measurements of the tubes.

**Figure 7**: Overview of curvature and ovalisation measurements during the tests. A photograph of the brackets is presented in Figure 6c.

### *3.3.2 Discrete measurements of tube geometry*

During the test, a trolley, driving on rails suspended above the specimen, monitors the development of geometrical imperfections by laser scanning a line profile of the specimen intrados. The trolley is able to deliver very precise measurements, but these measurements have to be corrected to account for the curvature of the specimen, as the rails did not curve with the specimen. An additional trolley on the inside of the specimen, performs line scans similar to the external trolley. As this trolley moves inside the bent tube, no correction to account for the bending curvature is necessary. A downside of this

method is the lower accuracy of the measurement, caused by the uneven driving surface of the trolley and the flawed laser reflection due for example dirt on the inside of the tube wall.

In addition to the longitudinal line scans, the internal trolley is also capable of performing circumferential scans of the tube which give information on actual shape of the cross section. Using very closely spaced circumferential scans, 3D images of the buckled section could also be obtained. As these internal and external scans require the specimen to be stationary, they are performed in between load steps. A sketch of the two trolleys and a photograph of the internal and external trolley is presented in Figure 8.

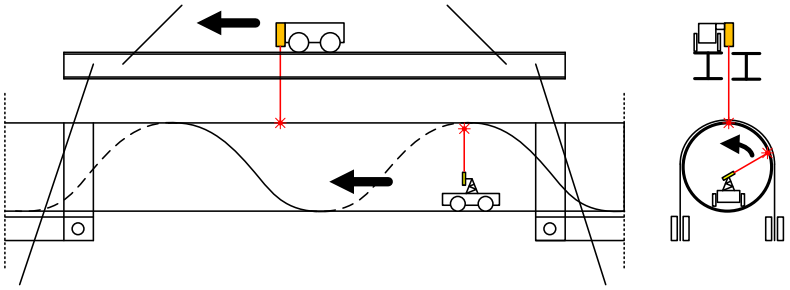

(a) Schematic overview of laser scanning during test

(b) Suspended rails with external laser trolley

(c) internal laser trolley

**Figure 8**: Overview of laser scanning during test.

## 4 RESULTS OF PRELIMINARY MEASUREMENTS

### 4.1 Tensile and compressive material properties

An overview of the results of the tensile tests on machined coupon specimens is presented in Table 2 in terms of tensile yield stress corresponding to 0.2% plastic strain. The results show that, on the average, the longitudinal yield strength is 6.7% higher than in hoop direction. Furthermore, the yield strength on the inside of the tube wall is about 3.7% lower than on the outside of the tube wall. These values differ among the tubular specimens, but show similarities among tubes which are deemed to originate from the same production batch.

As discussed in paragraph 3.2, tensile tests have been performed on strip coupon specimens extracted in the longitudinal and hoop direction, as well as on the inside and the outside of the tube wall. Since the main loading during the tests is in longitudinal direction, the reference yield strength of a specimen or specimen part is determined as the average yield strength of the machined specimens in the longitudinal direction. This reference yield strength is used for normalization purposes later in this paper, as well as in the companion paper (Part II).

| Specimen I.D. | Type | Inside of wall | | Outside of wall | |
|---|---|---|---|---|---|
| | | longitudinal | hoop | longitudinal | hoop |
| T1 | Plain | 510 | 508 | 555 | 584 |
| T2 | Plain | 401 | 379 | 412 | 374 |
| T3 Left | GW | 381 | 326 | 403 | 392 |
| T3 Right | | 431 | 374 | 436 | 393 |
| T4 | Plain | 427 | 389 | 455 | 408 |
| T5 | Plain | 419 | 411 | 379 | 400 |
| T6 Left | CCW | 550 | 508 | 505 | 534 |
| T6 Right | | 520 | 519 | 573 | 576 |
| T7 Left | GW/CCW | 605 | 497 | 622 | 585 |
| T7 Middle | | 614 | 452 | 594 | 573 |
| T7 Right | | 623 | 529 | 592 | 550 |
| T8 | Plain | 448 | 421 | 457 | 413 |
| T9 | Plain | 609 | 510 | 617 | 555 |
| T10 Left | GW/CCW | 527 | 476 | 559 | 538 |
| T10 Middle | | 521 | 450 | 489 | 486 |
| T10 Right | | 329 | 304 | 336 | 340 |
| T11 | Plain | 343 | 326 | 357 | 334 |
| T12 Left | GW/CCW | 453 | 416 | 441 | 421 |
| T12 Middle | | 499 | 472 | 516 | 467 |
| T12 Right | | 436 | 414 | 462 | 423 |
| T13 Left | GW | 440 | 403 | 446 | 412 |
| T13 Right | | 461 | 423 | 464 | 434 |

**Table 2**: Overview of measured tensile yield stress in MPa from machined specimens (

The comparison between the results obtained from the machined specimens and the full thickness specimens is good. Some examples of this comparison are presented in Figure 9. In case of different results obtained from the inside and the outside of the tube wall, the results from the corresponding full thickness specimens mostly lie in between. Since the circumferential full thickness specimens need to be flattened for testing, in many cases the sharp yield plateau boundary disappears, as shown in Figure 9d.

Considering the relatively small difference in material properties between the hoop direction and the longitudinal direction (see Table 2), it is unsurprising that the differences between the results of the full thickness specimens in the directions longitudinal and perpendicular to the original coil and the principal directions of the tube are rather small. Some influence of the flattening of the full thickness specimens in directions other than longitudinal creates some additional apparent anisotropy.

All specimens containing a girth weld or a coil connection weld consist of two or more specimen parts. The material behavior of these two parts is not equal, leading to a strong and weak side of the weld. Nevertheless, differences mostly have been relatively small. An exception is specimen T10, which consists of two specimen parts with a yield strength over 500 N/mm$^2$, and one weaker part with a yield strength of 333 N/mm$^2$ (see Figure 10). This large difference was not expected beforehand.

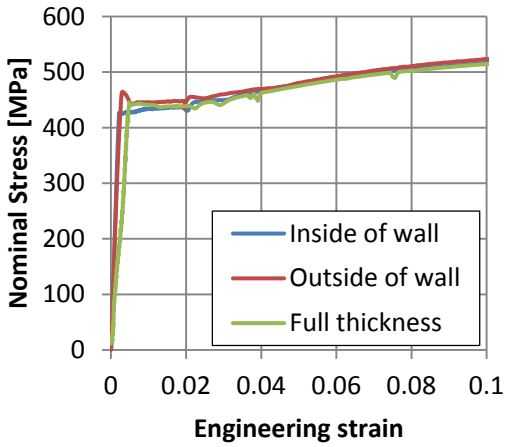


(a) T4 longitudinal direction

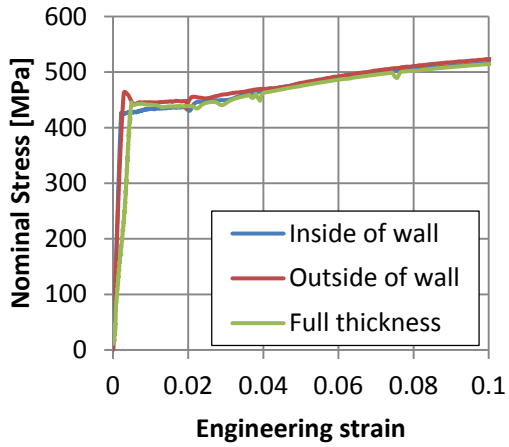


(b) T4 hoop direction

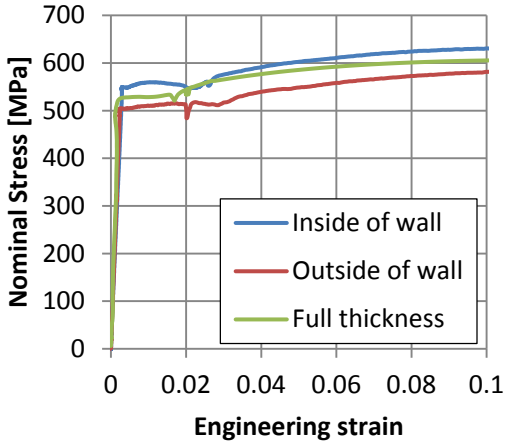


(c) T6Left Longitudinal direction

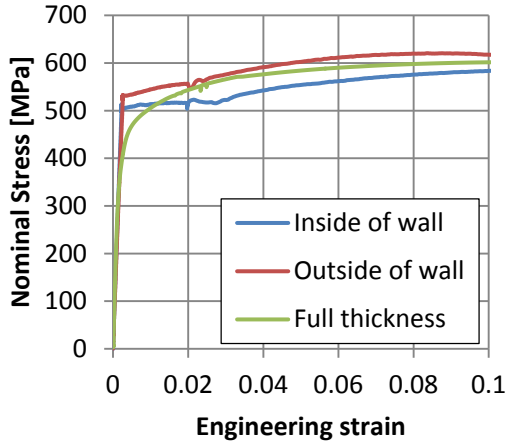


(d) T6Left hoop direction

**Figure 9**: Comparison of tensile tests from machined specimens with full thickness specimens for two specimen parts.

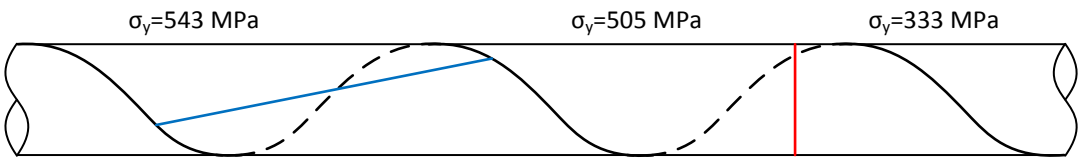


**Figure 10**: Sketch of specimen T10 featuring a girth weld connecting two specimen parts of significant different strength.

The strength of the weld material has also been measured by experimental testing. For a presentation of all results of the tensile tests on spiral weld material, the reader is referred to [29]. The average weld overmatch has been found to be 20% on yield strength and 19% on tensile strength. Ductility of the weld material has been found to be satisfactory with ultimate strain values ranging from 17% to 29%.

From each set of specimens with similar wall thickness, one specimen has been selected for compression tests. The stress in the specimens is, similar as in tensile tests, obtained from the applied force. The reported strain is the average from the three applied strain gauges (see Figure 4). Even though the compression specimens are supported against buckling, instability is unavoidable upon approaching or reaching the yield strength of the material, due to the extreme reduction in bending stiffness of the specimens in that situation. Since the specimens could not be observed during the test, the exact moment of buckling of the specimens could not be determined. However, bending in the specimen is detected by the three strain gauges. When one strain gauge starts deviating significantly from the other two, the specimen exhibits bending. This point is marked in the graphs. After this marker, the specimen may have been laterally instable to some extent.

One example of the full results of a compression test and its corresponding tensile test are presented in Figure 11. The figure shows the results of a compression and tensile test on specimen T1 in hoop direction on the inside of the tube wall. To compare the tensile and compression test results, the tensile test results are depicted both in the tensile and compression domain. It is clear that the comparison between the two results is excellent in this case.

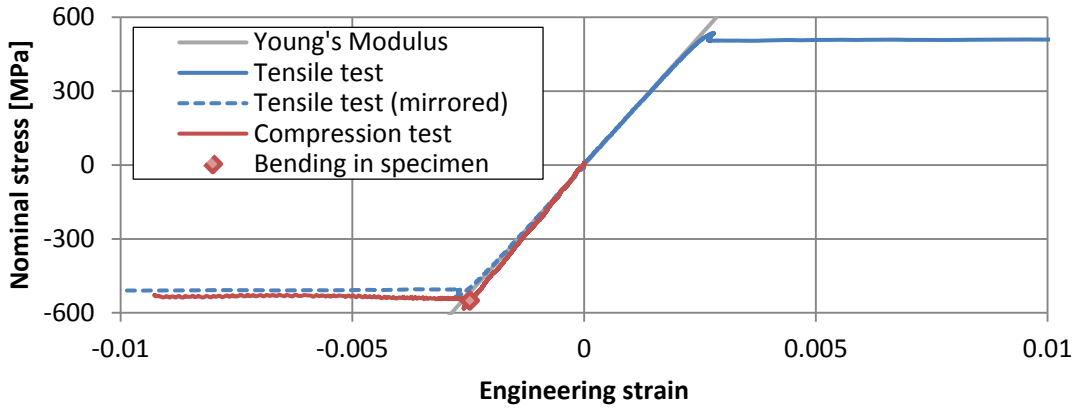


**Figure 11**: Results of compression and tension tests of specimens taken from specimen T1 in hoop direction on the inside of the tube wall.

Further compression tests are summarized in Figure 12. To enable a comparison between compression tests and tensile tests on specimens taken from the same tube in the same orientation (longitudinal or hoop) and location in the tube wall (inside or outside), the tensile test results are depicted in the compression domain. The results from the compression tests are quite similar to their tensile counterparts. Some specimens exhibit premature buckling, such as $T1_{long;inside}$. A few specimens show a Bauschinger effect due to the straining of the plate material during production. This behavior is most notable on the outside of the tube wall.

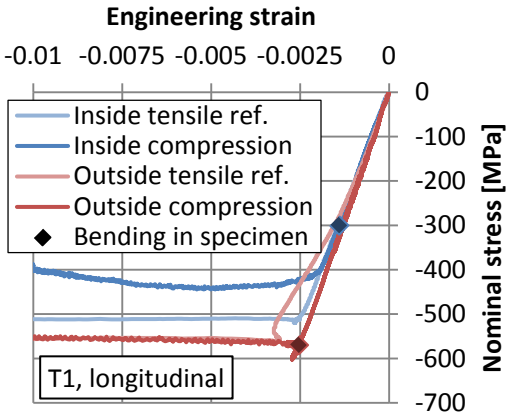


(a) T1 longitudinal direction.

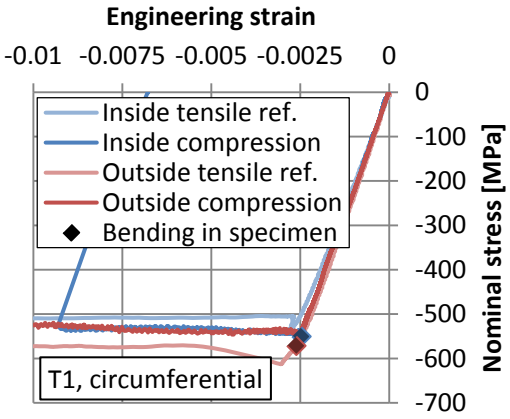


(b) T1 hoop direction

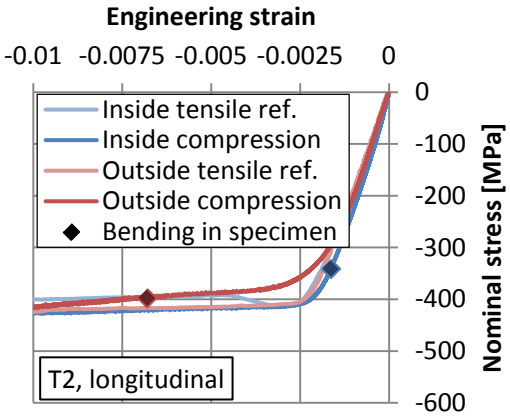


(c) T2 longitudinal direction

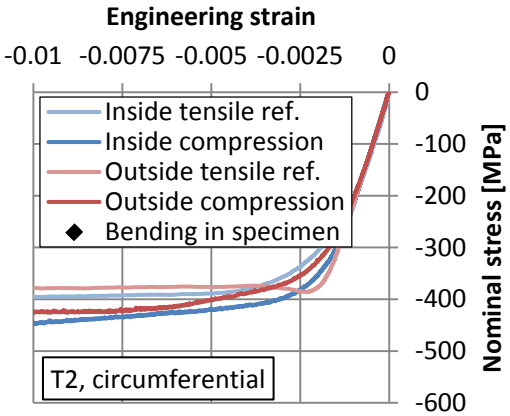


(d) T2 hoop direction

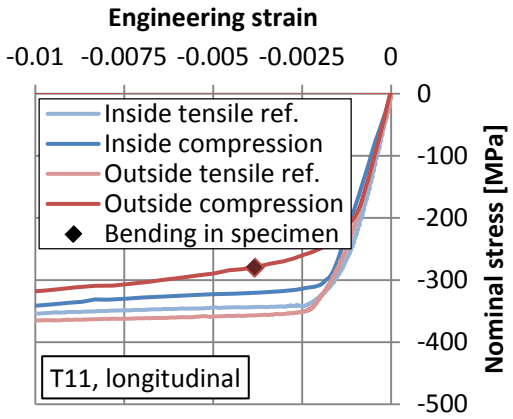


(e) T11 longitudinal direction

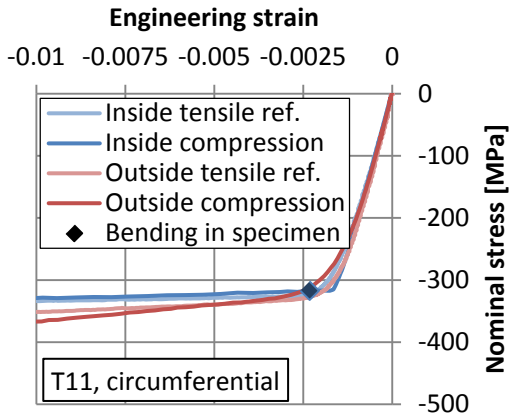


(f) T11 hoop direction

**Figure 12**: Results of compression tests compared with reference results of tensile tests on specimens extracted from the same tube in the same orientation. Results of tensile tests are depicted in the compression domain to facilitate comparison with the corresponding compression tests.

### 4.2 Measurements of wall thickness and diameter

The average measured wall thickness of each specimen is listed in Table 1. Using the sample mean and variance as best estimate for the true distribution of wall thicknesses over the tube, a mean and 95% confidence interval for the wall thickness of each specimen part is presented in Figure 13. The figure shows that the spread of the wall thickness is small within all specimen parts, which is to be expected since each specimen part is made of only one continuous steel plate.

A notable feature of specimen T10 (see Figure 10) is that part $T10_{right}$ has an average wall thickness of 12.8 mm, while the other parts of the specimen have an average wall thickness of 13.3 mm. Therefore, the right part is much weaker, considering also the differences in material properties.

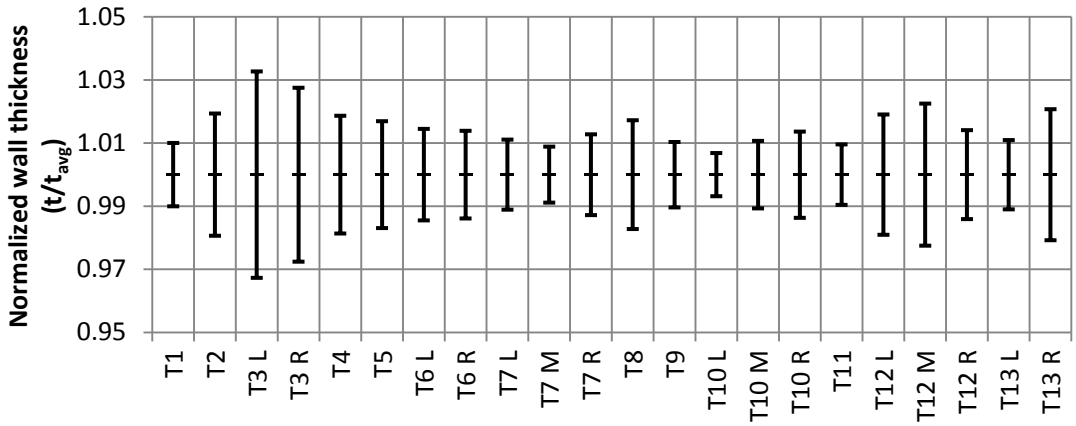


**Figure 13**: 95% confidence intervals of wall thicknesses in each specimen part, calculated under assumption of normal distribution.

The averaged results of all measurements across the original coil width of the specimen are presented in Figure 14. In similar fashion as in Figure 13, the mean and variance of the sample is used as best estimate for the true properties of the thickness distribution. From the figure can be concluded that there is a small but negligible drop in wall thickness towards the sides of the coil. Similar measurements towards the coil ends also show negligible thickness variations.

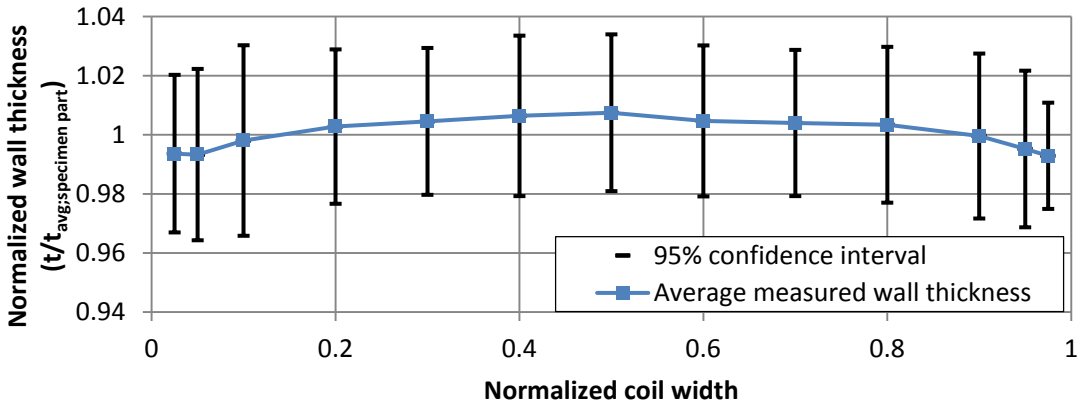


**Figure 14**: Measured thicknesses over original coil width, normalized by the average thickness of the corresponding specimen part. Average for all specimen parts. 95% confidence interval calculated the under assumption of normal distribution.

The average measured diameter of each specimen part is listed in Table 1. Aside from the average diameter, the initial ovalisation of the tube is recognized as a relevant parameter. The ovalisation parameter $f$ is defined as $(D_{max}-D_{min})/D_{ave}$. Before testing, the diameter of the specimens has been measured in four orientations at five cross sections. Given the initial measurement procedure, using brackets and tube rotation in fixed increments (see Figure 5), the minimum and maximum diameter of a given cross section are not necessarily measured, resulting in a lower bound estimate for parameter $f$. Alternatively, the initial ovalisation of the tubes can be obtained from the internal laser scan made at the start of the test, albeit with lesser accuracy due to causes discussed earlier.

In Figure 15, the average ovalisation and a 95% confidence of each specimen part is presented. In the measurements from the laser trolley, no distinction could be made between specimens parts. Therefore, the average of the full specimens is presented at the separate parts. Furthermore, no laser trolley measurements were available for T1 and T2. Considering the limited amount of data from the bracket measurements, the confidence interval is based solely on the laser trolley measurements. The confidence interval is calculated under the assumption that the mean and standard deviation calculated from the sample can be used as true parameters.

From Figure 15 can be concluded that the initial ovalisation of all specimens is very small. For example, in design according to DNV offshore standards for pipelines, a minimum value of 0.005 must be used for $f$ [31]. The mean values of the measurements are, with one exception, all lower than this minimum value.

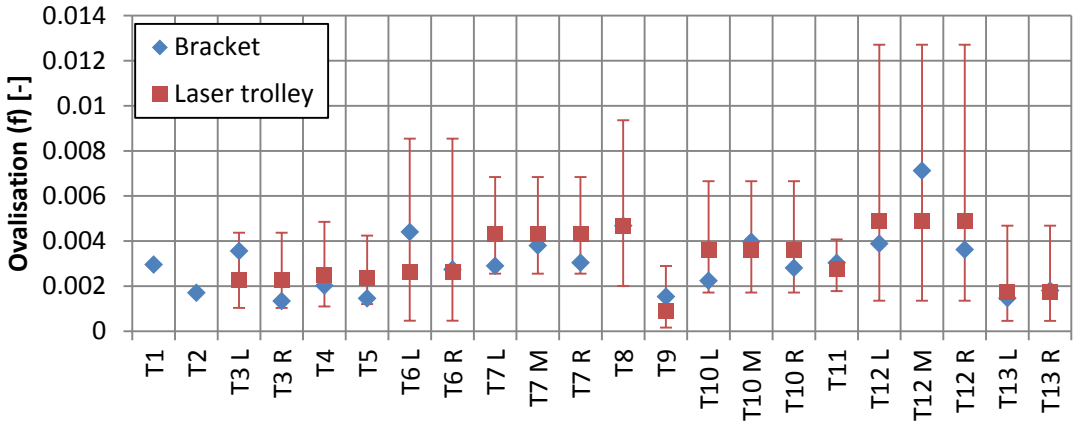


**Figure 15**: Average ovalisation parameters of each specimen part. 95% confidence interval calculated under assumption of lognormal distribution.

## 4.3 Measurements of initial imperfections

In the analysis of thin-walled shells with large values of $D/t$ ratio, initial geometrical imperfections are considered a paramount factor in determining the resistance against local buckling [32]. Although the tubes considered in the present work have significantly lower values of $D/t$ ratio than the shells considered in shell buckling analysis, initial imperfections are expected to have an influence on buckling location and bending moment capacity. Therefore, the orientation of the tube during the bending test has been based on the initial imperfections. For "plain" tubes, i.e. tubes without girth or coil connection welds, the longitudinal scan with the largest observed imperfection has been placed in maximum compression, with the exclusion of accidental damage such as dents. For tubes featuring a coil connection weld or girth weld, the occurrence of imperfections at these welds dictated the tube orientation during the bending test. For numerical analysis of the bending tests, the measured initial geometry will be used to provide a realistic range of imperfection amplitudes in the numerical models, as described in the companion paper [30].

### *4.3.1 "Plain" spiral-welded tubes*

The surface scans of the spiral-welded tubes have several notable characteristics that are observed in all spiral-welded specimens. In a segment between two spiral welds, the tube wall surface is not flat, but shows a series of local "hills" and "valleys". An example of an initial laser scan is depicted in Figure 16 for specimen T2. The graph represents a laser scan of the outer surface of the tube. All area the graph represents space outside the tube, the area beneath the graph represents the tube wall or space inside the tube. Neglecting the variation of thickness (see Figure 14), the scanned surface can be assumed to represent the initial imperfect configuration of the middle surface of the shell. At the location of spiral weld, the scan includes the weld bead, meaning that, at these locations, the scanned surface does not represent the middle surface. This results in the sharp peaks that at the location of the spiral welds.

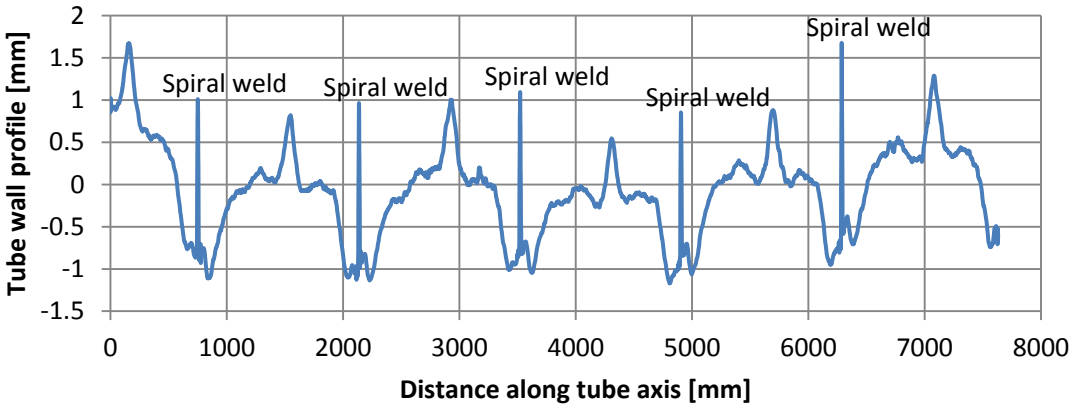


**Figure 16**: Initial imperfection geometry of specimen T2 at orientation 0º. The sharp spikes mark the presence of a spiral weld.

It appears that in between the spiral welds, a quasi-repeating tube wall profile pattern is present. This is attributed to the fact that the wavy imperfections may be the result of the manufacturing process. As described in chapter 2 and modeled in Part II [30], spiral-welded tubes are cold formed by means of a three-roller system that bends the steel coil. Should these rollers be not continuous but discrete, a series of discrete imperfections may be the result, as seen in Figure 16. After forming the material, the tube is supported on several smaller, but certainly discrete, rollers. These rollers might also have an influence on to the observed initial imperfection profile.

Upon closer inspection it appears that some of the tubes feature visible marks of rollers on the outside of the wall, running parallel to the spiral welds (see Figure 17). When these marks are lined up with a measurement of initial imperfections, it can be concluded that the imperfections are indeed caused by these rollers (see Figure 18). Over time these roller marks are no longer visible by the naked eye due to wear of the tube's surface, although the corresponding geometrical imperfections remain. As a result, not every specimen showed these markings. Furthermore, when the markings are visible, most of them are very vague. It is therefore possible that, although not every imperfection peak matches with a roller mark, these rollers have a significant influence on the observed quasi-repeating imperfections. In this study, it is assumed that all the observed quasi-repeating geometrical imperfections are caused by the cold-forming process.

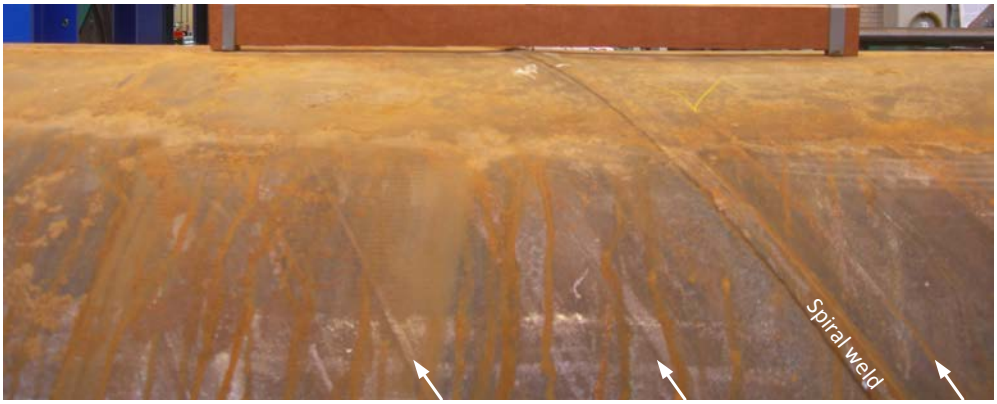


**Figure 17**: Photograph of specimen T1 featuring roller marks. The visible marks are indicated with arrows.

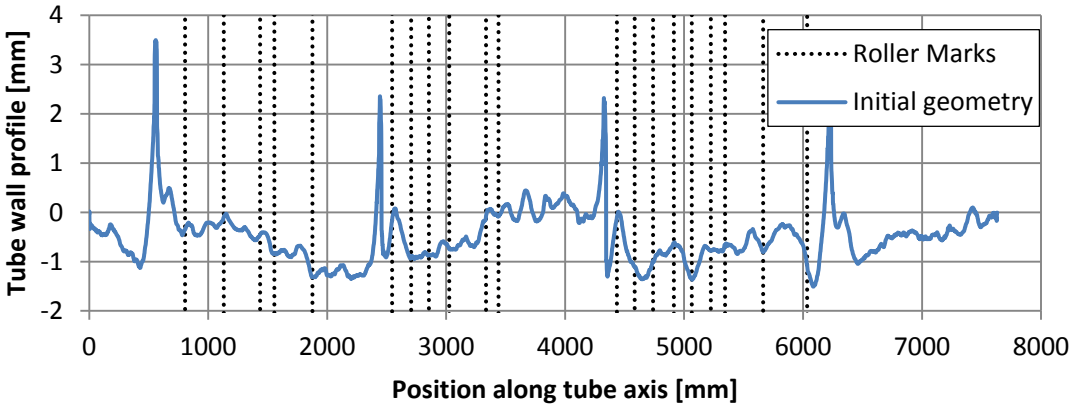


**Figure 18**: Initial imperfection geometry of specimen T1 at cross-sectional orientation 0º with roller mark overlay. The roller marks coincide with the "waves" of the geometric imperfection pattern.

A collection of the initial imperfection depth at the local buckle area of each "plain" tube is presented in Table 3. Two examples of the procedure to determine this imperfection size are presented in Figure 19. On average, the initial imperfection has a depth equal to 6.6% of the wall thickness of the tube. A full study into the dominant geometrical imperfection modes and their amplitudes, using Fourier series analysis, is documented elsewhere [33].

| Specimen I.D. | $D$ [mm] | $t$ [mm] | $D/t$ [-] | Imp/$t$ [%] |
|---|---|---|---|---|
| T1 | 1066 | 16.4 | 65.1 | 3.6 |
| T2 | 1067 | 9.0 | 118 | 9.0 |
| T4 | 1065 | 9.2 | 116 | 6.0 |
| T5 | 1070 | 9.0 | 118 | 7.2 |
| T8 | 1068 | 9.1 | 117 | 11.6 |
| T9 | 1069 | 16.3 | 65.4 | 9.2 |
| T11 | 1068 | 12.9 | 83.0 | 6.2 |

**Table 3**: Overview of initial imperfection sizes at the local buckling location.

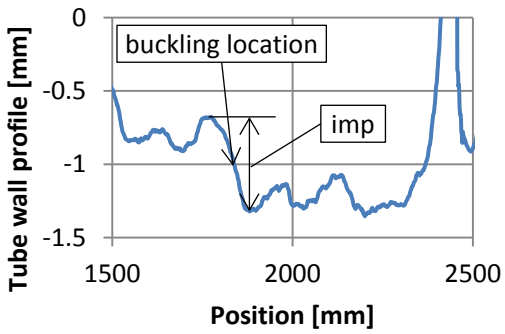


(a) Measurement of imperfection for tube T1; for full tube wall profile see Figure 18

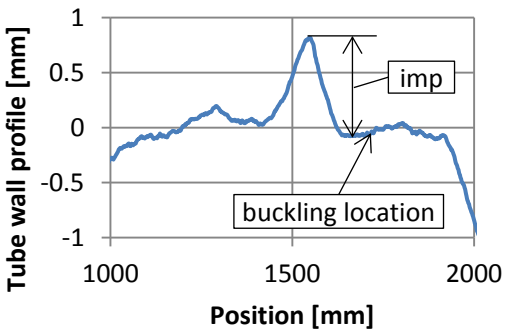


(b) Measurement of imperfection for tube T2; for full tube wall profile see Figure 16

**Figure 19**: Examples of measurement of imperfection size at buckling location.

### *4.3.2 Tubes with girth and coil welds*

The presence of girth or coil connection welds may introduce additional imperfections that, if exceeding certain values, may result in local buckling at these welds. In pipeline applications, tubes connected by girth welds are usually aligned with internal clamps and welded fully automatically, but in many structural applications, the use of advanced clamping equipment to avoid any misalignment is not as common. Furthermore, manual welding may take place on site. Therefore, misalignments at the girth weld are expected to occur. On the other hand, welding of the coil connection weld is performed in a controlled environment in the spiral mill (see section 2), so that misalignment is far less likely to occur. For both welds, the formation of additional geometrical imperfections due to weld shrinkage is possible.

A comparison of initial imperfections at girth welds is depicted in Figure 20 and Figure 21. Similarly as in the profile diagrams of plain tubes, the lines can be assumed to represent the middle surface of the shell, with the exception of weld caps. The comparison shows that misalignments can be as large as 3 mm, which is 33% of the plate thickness for that specific specimen. It is also visible that near the weld an inward geometrical imperfection is formed, probably due to weld shrinkage. Figure 22 and Figure 23 show the initial imperfections near coil connection welds. Apparently the coil connection welds have the tendency to bulge outwards of the tube. The imperfections of these welds appear to be larger than the geometrical imperfections caused by spiral welding. For example, Figure 22 includes a scan of a spiral weld in the line representing specimen T7 and Figure 23 includes a scan of a spiral weld in the line representing specimen T10.

The coil connection weld in specimen T6 is not bulging outwards but shows a profile bending inwards (see Figure 22). Considering that the top of the weld bead coincides exactly with the surrounding plate material, it is likely that this weld has been forced inwards during manufacturing, transportation or storage. In addition, this specimen also shows a small misalignment at the coil connection weld. From every specimen, laser scans are available at several cross-sectional orientations

(see Figure 5). The displayed geometries of the girth welds and coil connection welds in Figure 20 - Figure 23, are not necessarily the ones placed in the intrados of the specimen during the bending test.

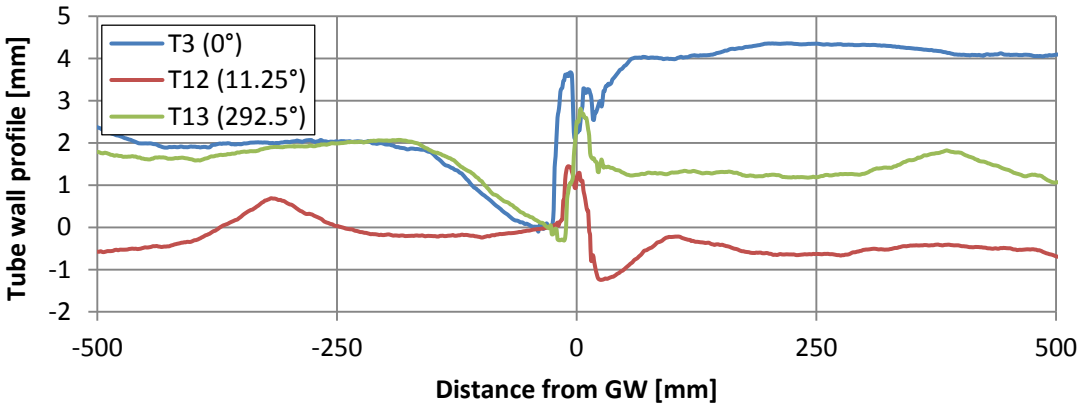


**Figure 20**: Comparison of geometrical imperfections in the vicinity of a girth weld for three tubes with wall thickness 9 mm.

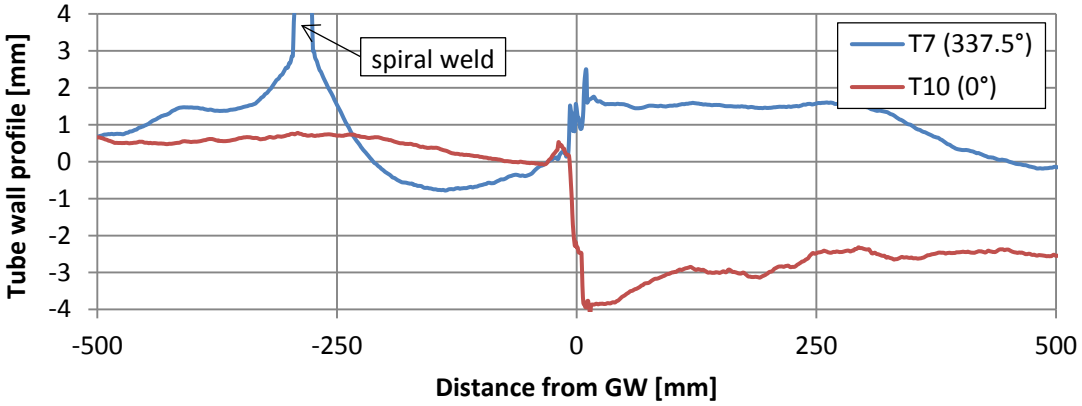


**Figure 21**: Comparison of geometrical imperfections in the vicinity of a girth weld for tube T7 with wall thickness 16 mm and T10 with wall thickness 13 mm.

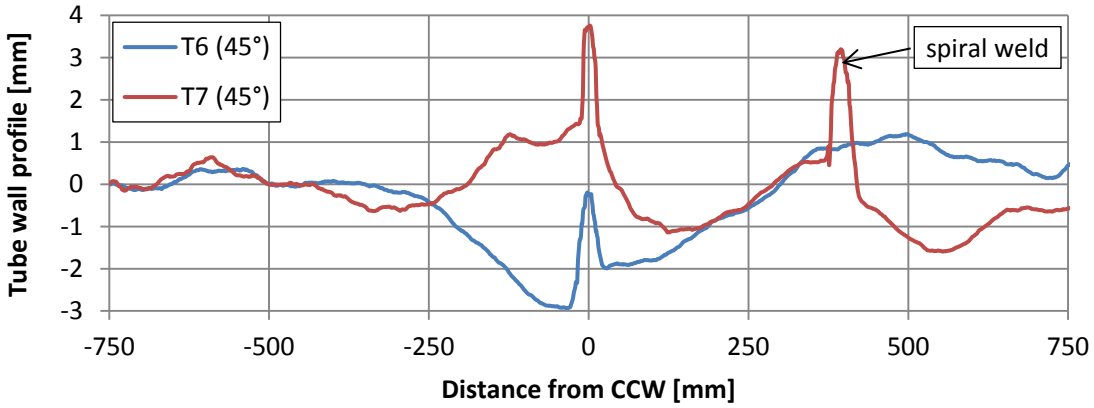


**Figure 22**: Comparison of geometrical imperfections close to a coil connection weld for tubes with wall thickness 16 mm. Note that the scan of tube T7 in this figure and Figure 21 are made at different cross-sectional orientations (see Figure 5).

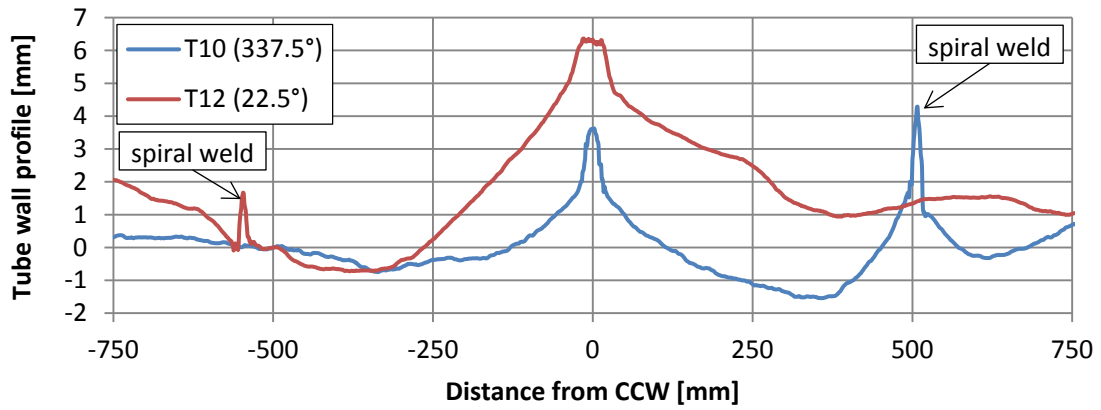


**Figure 23**: Comparison of geometrical imperfections close to a coil connection weld for tube T10 with wall thickness 13 mm and tube T12 with wall thickness 9 mm.

Figure 20 - Figure 23 show a combination of initial imperfections in shapes of hills and valleys and misalignments at these girth welds and coil connection welds. The overall geometrical imperfection can mostly be described by one measurement, similarly as has been performed for the plain tube sections. For reasons of efficient numerical modelling all imperfections of the tubes containing a girth weld or coil connection weld are documented as such [30]. A collection of the depths of these imperfections at the location of the local buckle is presented in Table 4. Two examples of the procedure used to determine this imperfection size are presented in Figure 24. On average, an imperfection of 19.2% of the tube wall thickness is found, which is almost three times as large as the average imperfection found in plain tubes. In two specimens (T7 and T12), local buckling took place away from the girth weld or coil connection weld. In these cases, the imperfection documented in Table 4 is therefore an imperfection in a plain tube section. As expected, these two initial imperfections are lower than the initial imperfections found at the girth welds and/or coil connection welds of the other tubes.

| Specimen I.D. | $D$ [mm] | $t$ [mm] | $D/t$ [-] | Imp/$t$ [%] |
|---|---|---|---|---|
| T3 (GW) | 1069 | 9.0 | 118 | 20.0 |
| T6 (CCW) | 1066 | 16.3 | 65.3 | 18.6 |
| T7* (GW/CCW) | 1068 | 16.3 | 65.4 | 11.0 |
| T10 (GW/CCW) | 1070 | 13.1 | 81.6 | 27.4 |
| T12* | 1069 | 9.1 | 117 | 12.7 |
| T13 (GW) | 1070 | 9.2 | 117 | 25.5 |

**Table 4**: Overview of initial imperfection sizes. **Imperfection in plain tube section*

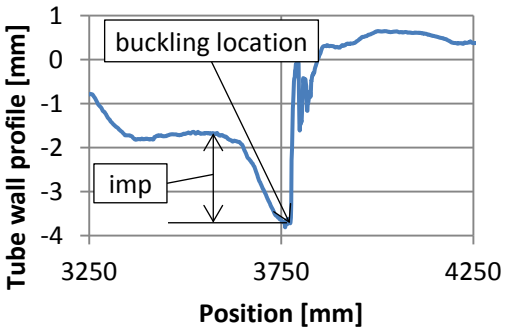


(a) Measurement of imperfection for tube T3; for tube wall profile also see Figure 20.

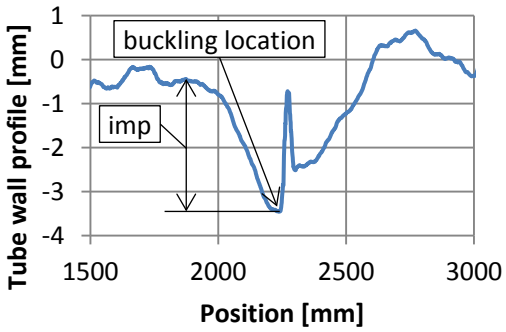


(b) Measurement of imperfection for tube T6; for tube wall profile also see Figure 22.

**Figure 24**: Examples of measurement of imperfection size at buckling location near a girth weld or coil connection weld.

## 5 RESULTS OF FOUR-POINT BENDING TESTS

As a result of the bending loads exerted, all specimens have failed in the form of local buckling. The specimens with $D/t$ equal to 120 failed suddenly and violently. In contrast, the transition between a stable and unstable tube wall has been much more gradual for the thick walled specimens. Especially the thick walled specimens with large initial imperfections, such as specimen T6 (see Figure 22) have had a very smooth transition between the pre-buckling stage and post-buckling stage. Some of the sudden failures of the thin walled specimens resulted in failure of some of the more sensitive measurement equipment. In these cases, the post buckling stage of the response has been removed from the corresponding moment-curvature diagrams.

In most cases, the local buckle configuration consists of one main buckle with two adjacent secondary buckles which form after little further deformation of the specimen. Some examples of local buckling shapes are presented in Figure 6d and Figure 25 - Figure 27 . By using the data of the internal radial laser scan (see Figure 8), the shapes of the buckles are depicted clearer with 3D images. The images show that for more slender specimens, the local buckling shape is much sharper (compare Figure 26 and Figure 27).

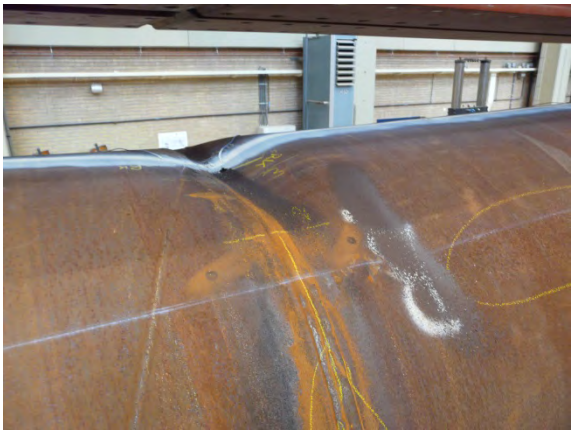

(a) Photograph of buckle

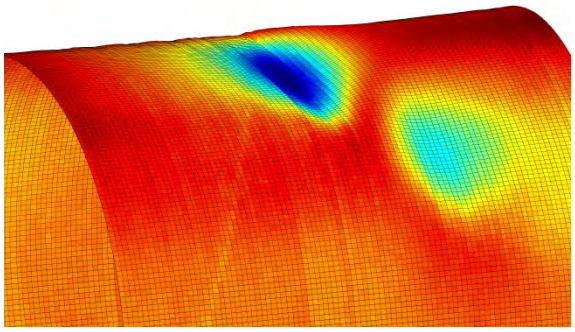

(b) 3D scan of buckle

**Figure 25**: Local buckle of tube T3 ($D/t$=118) at the girth weld.

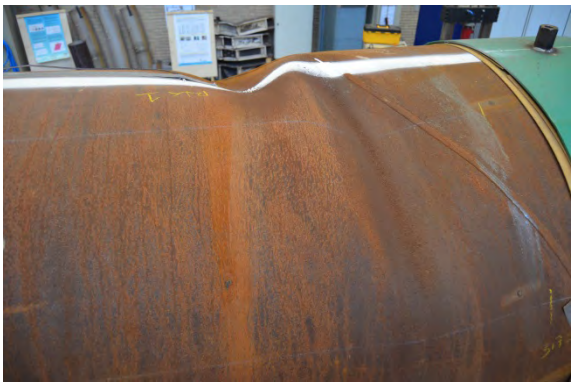

(a) Photograph of buckle

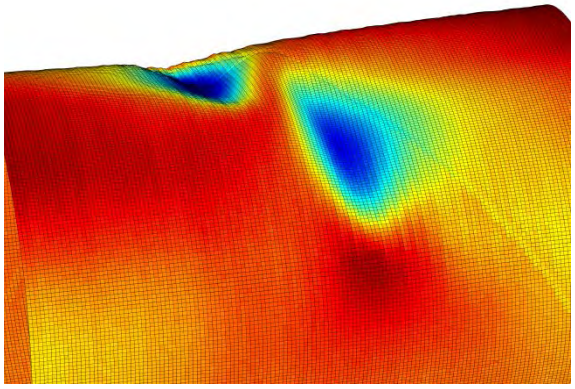

(b) 3D scan of buckle

**Figure 26**: Local buckle of tube T7 ($D/t$=65.4). The buckle initially occurred away from the spiral weld; under further deformation, buckles extend past the spiral weld.

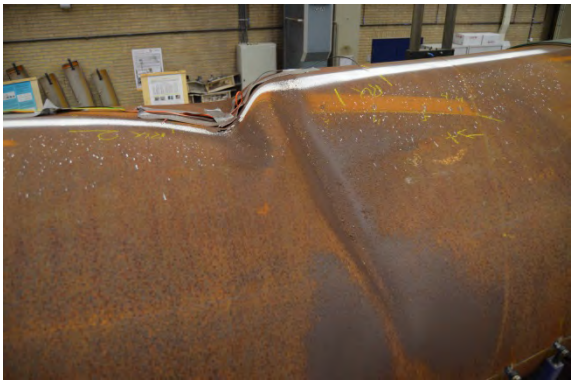

(a) Photograph of buckle

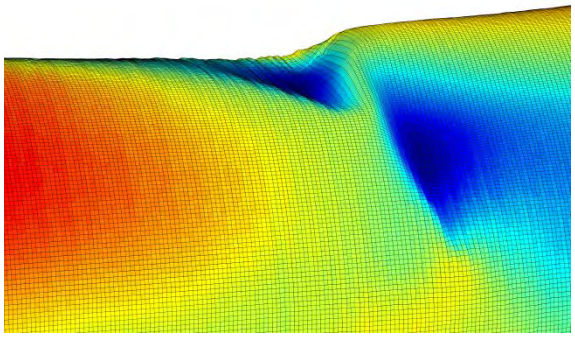

(b) 3D scan of buckle

**Figure 27**: Local buckle of tube T12 ($D/t$=117) at final deformation stage of the specimen.

## 5.1 Moment-curvature diagrams

Two typical results of plain tubes are shown in Figure 28. The diagrams present the moment in relation to the local curvature measurements and the average curvature measurement (see Figure 7). From the figure is clear that the thicker specimens (1067x15.9 mm) have much a more pronounced deformation capacity than the thinner specimens (1067x9.0 mm). Furthermore, this plastic deformation is not evenly distributed over the tube segment with constant moment. Clearly, the curvature measured by bracket $\kappa_1$ is higher than the average and the curvature obtained from other local measurements in Figure 28a, well before the maximum bending moment is reached or a local buckle forms. In case of thinner specimens, differences between the curvature measurements are smaller, but still present. Apparently the bending moment capacity of the tube is varying over the length of the specimen.

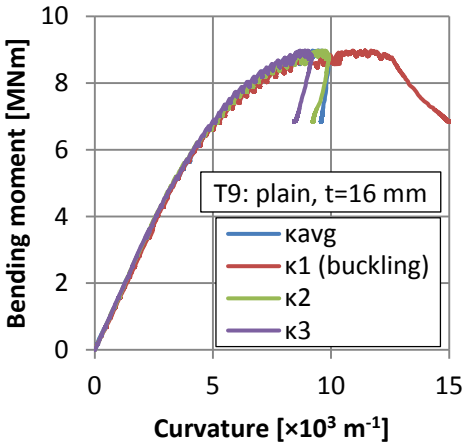


(a) Specimen T9 ($D/t$=65.4)

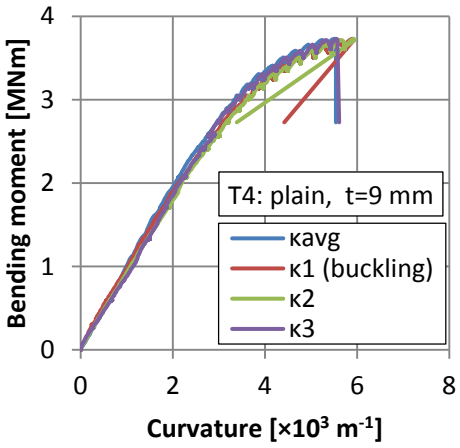


(b) Specimen T4 ($D/t$=116)

**Figure 28**: Examples of moment-curvature diagrams for two typical specimens. Local buckling takes place within the local measurement marked with "(buckling)".

The bending behavior of all tubes is collected in graphs presenting the moment curvature diagrams of specimens of similar wall thickness and material properties (see Figure 29). In case of the specimens with a wall thickness of 9 mm, the specimens are grouped with specimens with similar behavior. The horizontal axes are normalized by curvature parameter $\kappa_1$ defined as $\kappa_1=t/D^2$. The vertical axes are normalized by the plastic bending moment capacity of the cross section. In both cases, the specimen properties at the location of the local buckle are used for this normalization.

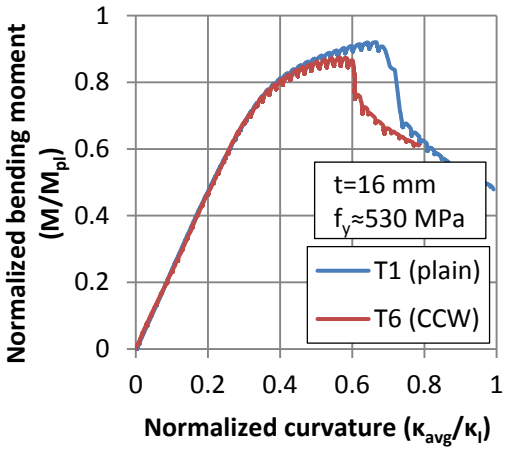


(a) Tubes with $t$=16 mm and $\sigma_y$≈530 MPa.

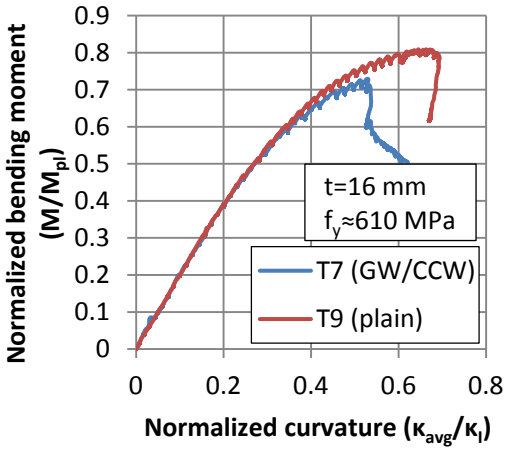


(b) Tubes with $t$=16 mm and $\sigma_y$≈610 MPa.

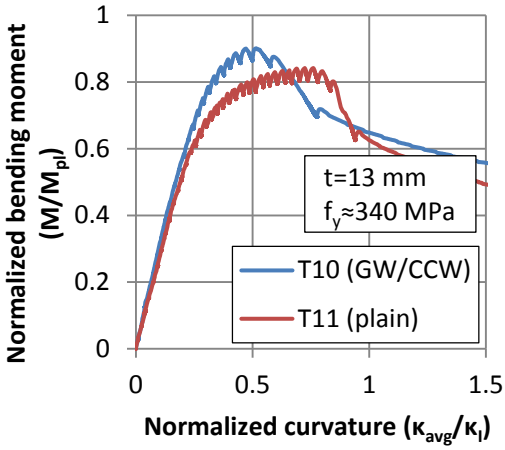


(c) Tubes with $t$=13 mm and $\sigma_y$≈340 MPa.

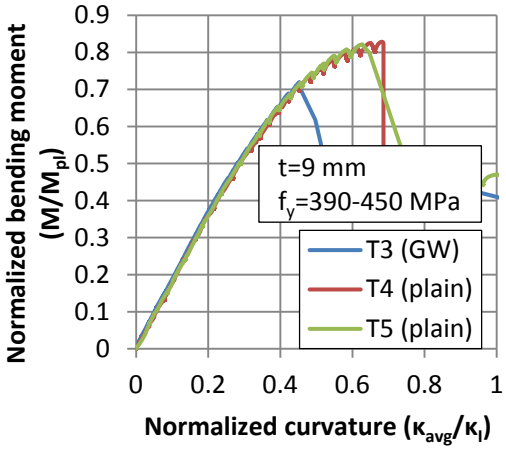


(d) Tubes with $t$=9.0 mm and $\sigma_y$=390-450 MPa.

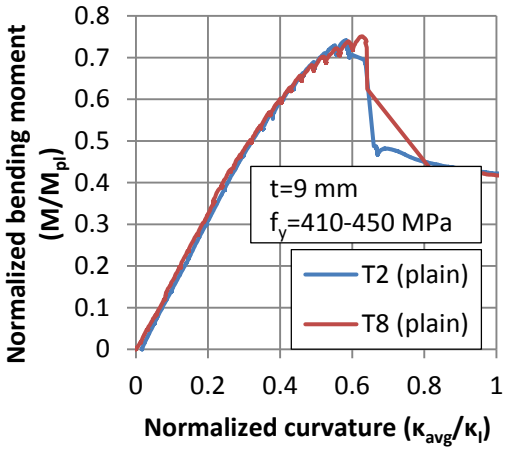


(e) Tubes with $t$=9.0 mm and $\sigma_y$=410-450 MPa.

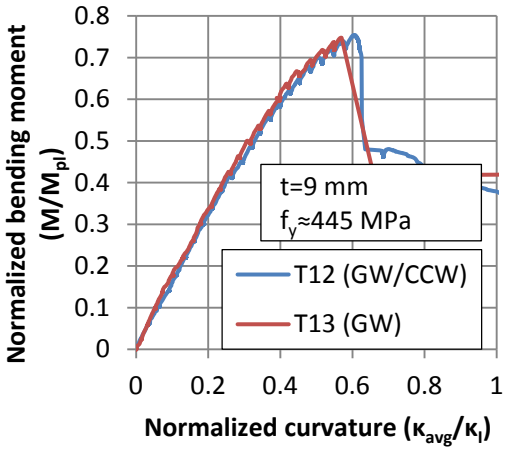


(f) Tubes with $t$=9.0 mm and $\sigma_y$≈340 MPa.

**Figure 29**: Moment-curvature diagrams of all spiral-welded specimens.

The results show that all specimens containing a girth weld or coil connection weld have lower performance than their plain counterparts, both in terms of maximum moment capacity and maximum curvature. Only Figure 29e and Figure 29f indicate that plain specimens may have a structural response similar to the specimens containing an additional weld. In any case, the additional welds appear to penalize the structural strength and deformation capacity. Possible causes for this are discussed in paragraph 5.5.

An exception to the above general observation is specimen T10. As discussed in section 4.1, this specimen features one specimen part that is significantly weaker than the attached other two. Since local buckling took place in the weak part very close to the girth weld where it was connected to a stronger part, a significant supporting effect of the attached stronger specimen part is to be expected. This support results in higher resistance against buckle formation, due to a thicker wall and higher yield strength of the adjacent part, but also a higher resistance against ovalisation. A cross section with less ovalisation is less prone to local buckling, due to the smaller local radius of the tube cross section. Furthermore, the average curvature of the specimen is heavily influenced by the thicker specimen parts away from the buckle. These two effects lead to a relatively low critical average curvature in combination with a high maximum bending moment in Figure 29c.

## 5.2 Results of ovalisation measurements

Ovalisation measurements, performed during the tests, also provide useful information on the behavior of the specimens under consideration. Typical results of these measurements are presented in Figure 31 and Figure 32. In both figures, the overall development of the horizontal ovalisation of the specimen with respect to curvature is presented on the left. In all tests, the formation of a local buckle led to sudden increase of horizontal ovalisation near the buckling location. Further away, the horizontal ovalisation slightly decreased after local buckle formation, corresponding to the reduced curvature in these areas due to the decreased bending moment. Interestingly, also before bifurcation the ovalisation of the tube around the location of the local buckle is higher than in other parts of the tube. This feature is not only clearly visible in Figure 31 and Figure 32 but in almost all tests.

The graphs in Figure 31b and Figure 32b present a profile of ovalisation over the length of the test specimens at a curvature close to the critical curvature. The graphs provide a comparison between the measured ovalisation with external brackets (see Figure 7b) and the measurements performed by the internal laser scans (see Figure 8). The figures show that there is good agreement between these two measurement methods. The profiles of both tubes show that the specimen ovalisation is slightly reduced toward the middle supports. This effect is caused by a slight restriction of ovalisation by the load application straps at the middle supports. The initially parallel steel straps are deformed by the ovalizing tube, leading to an restriction of ovalisation (see Figure 30). Furthermore, the two outer ‘loading arms’ of the specimens are curved less and therefore support the middle area of the tubular specimen.

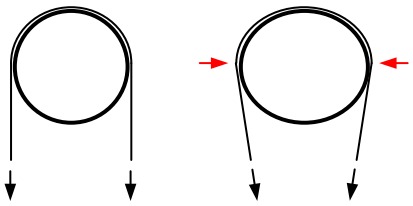

**Figure 30**: Restriction of ovalisation by middle supports.

Figure 31b and Figure 32b show that ovalisation is clearly higher at the location where local buckling would occur during the bending test. This locally higher ovalisation could induce local buckling at these locations, since the ovalisation increases the local radius of the shell cross section in the compression area of the tube. The fact that the local radius of the shell greatly influences the resistance to local buckling is well known [32]. On the other hand, a locally larger bending curvature at these locations due to differences in yield strength and tube wall thickness over the specimen length can be the underlying cause of both a larger ovalisation and earlier local buckling at these locations. In any case, tube ovalisation appears to be a good predictor of the buckling location.

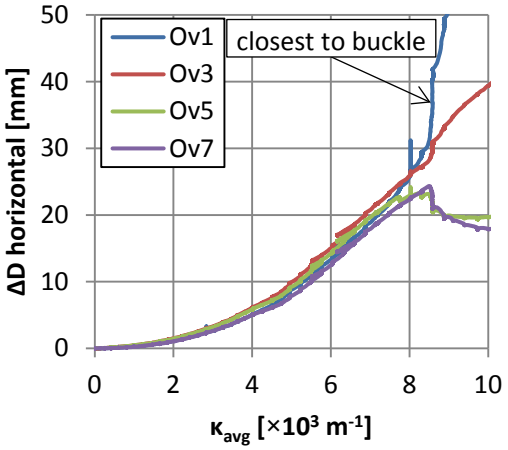


(a) Measured ovalisation with brackets. Selection of bracket results displayed.

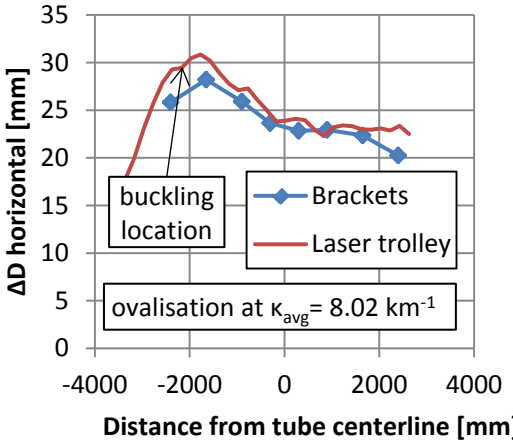


(b) Comparison between measurements from brackets and internal laser trolley.

**Figure 31**: Ovalisation measurements of test T6.

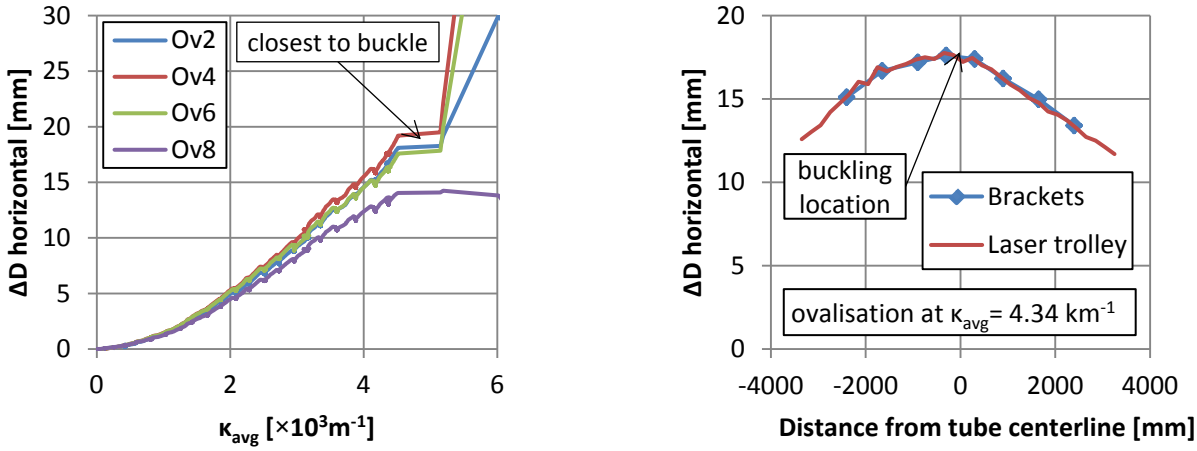


(a) Measured ovalisation with brackets. Selection of bracket results displayed.

(b) Comparison between measurements from brackets and internal laser trolley.

**Figure 32**: Ovalisation measurements of test T13.

### 5.3 Ultimate bending moment and deformation capacity

In the present work, instability is defined on the moment-curvature path at the point where the maximum bending moment occurs. Therefore, the critical values of curvature, strain and bending moment are obtained at this point. In a load-controlled situation, instability evidently occurs at this maximum of the resisted bending moment. In deformation controlled situations, such as the performed tests, it is possible to retain a stable situation at slightly higher curvatures and lower bending moments. In practice, the occurrence of a maximum bending moment is mostly associated with rapid concentration of curvature and local buckling, resulting in structural failure.

An overview of the maximal resisted bending moments is depicted in Figure 33. As suggested in structural design and analysis standards and recommendations [34] [35], the cross-sectional slenderness of the tubes is normalized by both the geometric slenderness ($D/t$) and the element's yield strength. In this case, the slenderness is normalized by $D/(t\varepsilon^2)$ with $\varepsilon^2=235/\sigma_y$, as suggested in [35]. The maximum bending capacity of specimens containing a girth or coil connection weld is, generally, equal or lower than their plain counterparts, with the exception of specimen T10 due to the strong discontinuity of cross-sectional properties.

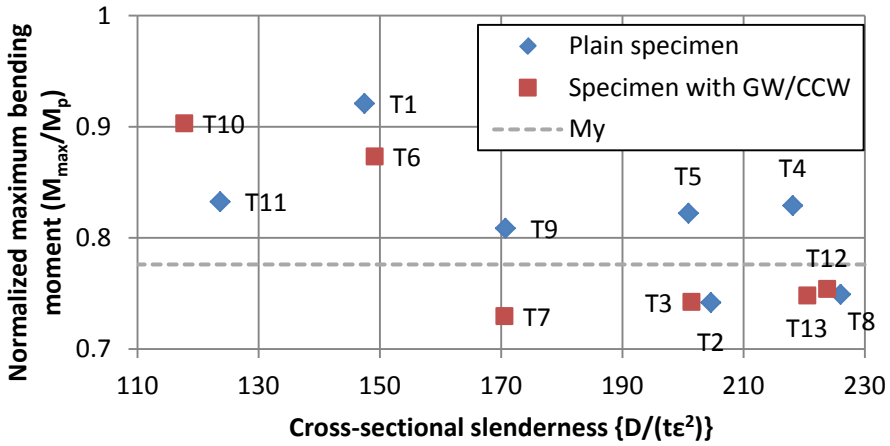


**Figure 33**: Maximum bending moment capacity of specimens. $M_y$ is defined as first yield moment of a non-ovalizing tube.

An overview of the strains attained at maximum moment is depicted in Figure 34. To avoid local wall bending effects, the reported strain is calculated from measured curvatures and nominal diameter instead of strain gauges; $\varepsilon=\kappa \cdot D/2$. Figure 34 shows the critical strain calculated from average curvatures; any curvature localization is thus not included in the graph. Considering the common practice in pipeline engineering to relate the critical strain to *D/t* as cross-sectional slenderness parameter [31], this approach has also been used in Figure 34. In the graph a detrimental effect of the presence of girth welds and coil connection welds is visible, similar as in the case of Figure 33. From Figure 33 and Figure 34 can be concluded that the specimens featuring a girth weld or coil connection weld have a lower bending moment and deformation capacity.

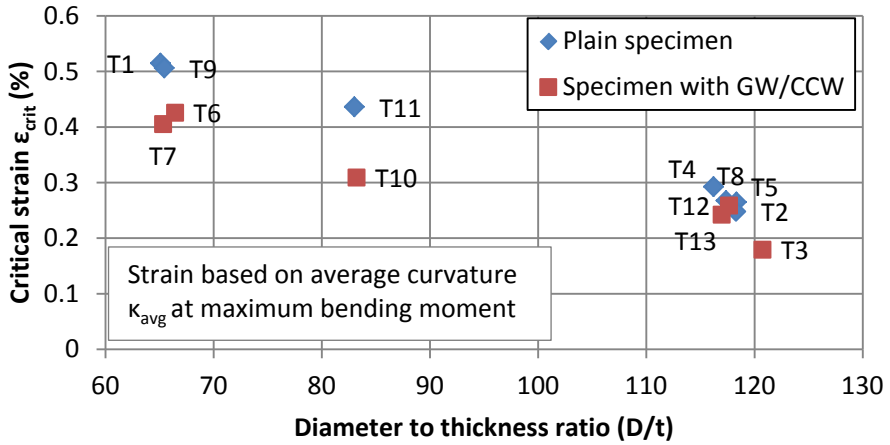


**Figure 34**: Critical strains based on average curvatures at maximum moment.

As shown in Figure 28, even before the maximum bending moment is reached, differences between locally measured curvatures and globally measured average curvatures arise. The ratio between the local curvature at the buckling location and the global curvature, both determined at the maximum bending moment, is presented in Figure 35. The results show that the local curvature is significantly higher than the average curvature in almost all cases. Exceptions are specimens T11 and T12, where curvature localized away from the buckling location. If instead of the local curvature at the buckling location, the maximum local curvature is used to determine the ratio, the data is in accordance with the other results. In that case, the curvature localization ratio ($\kappa_{local}/\kappa_{global}$) for specimens T11 and T12 is equal to 1.09 and 1.10 respectively.

Using the maximum local curvature for specimens T11 and T12, the curvature localization ratio ($\kappa_{local}/\kappa_{global}$) at maximum bending moment, averaged over all specimens, is 1.12. When reaching the maximum bending moment, the locally measured curvature is on average thus 12% higher than a globally measured average curvature, even though the applied bending moment is constant in the specimen section between the middle supports. Furthermore, it is noteworthy that the amount of curvature localization is hardly correlated with the tube slenderness and that curvature localization seems to be a little higher for specimens containing a girth weld or coil connection weld.

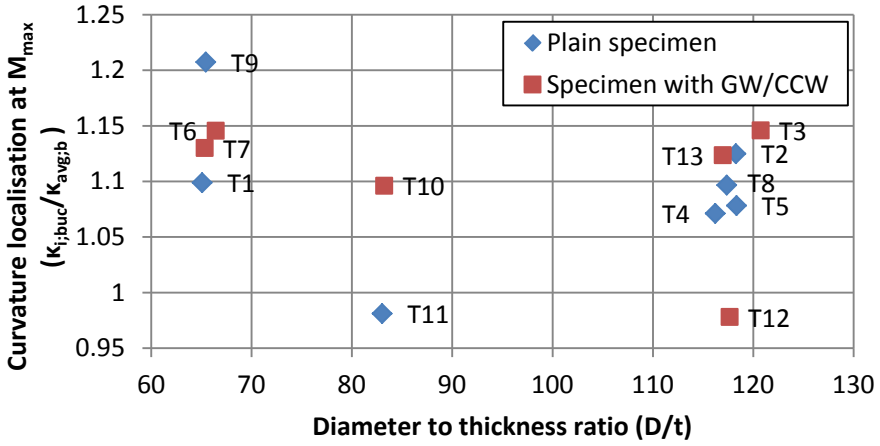


**Figure 35**: Comparison of local curvature at buckling location and global curvature at maximum moment.

In all previous analyses, the buckling moment of each specimen has been defined as the moment where maximum bending resistance is reached. Alternatively, buckling can be defined at the curvature where the resisted bending moment suddenly drops. It may be expected that for specimens with high $D/t$ ratio these two definitions provide the same result, while for specimens with low $D/t$ ratio there may be a certain difference. Figure 36 presents the ratio of curvatures at maximum bending moment and load drop-off, which is recognized as a measure of global ductility of the tubular specimen. In these analyses, the average curvatures have been used.

Using the geometric slenderness of the specimens ($D/t$), no correlation between ductility and slenderness is found (Figure 29b). However, if the cross-sectional slenderness parameter $D/(t\varepsilon^2)$ is

used, it appears that less slender specimens result in a higher ductility (Figure 29a). It must be noted that beyond a certain threshold value, further increase of slenderness does not seem to lead to further decrease of ductility. Naturally, a ductility of unity is the minimum, as this indicates that maximum bending moment and load drop-off occur simultaneously. Both graphs in Figure 36 show that also in terms of ductility, the presence of a girth weld or coil connection weld seems to penalize the bending capacity of the tubular member. However, if instead of a global curvature, the locally measured curvature is used to determine this ductility parameter, these differences disappear.

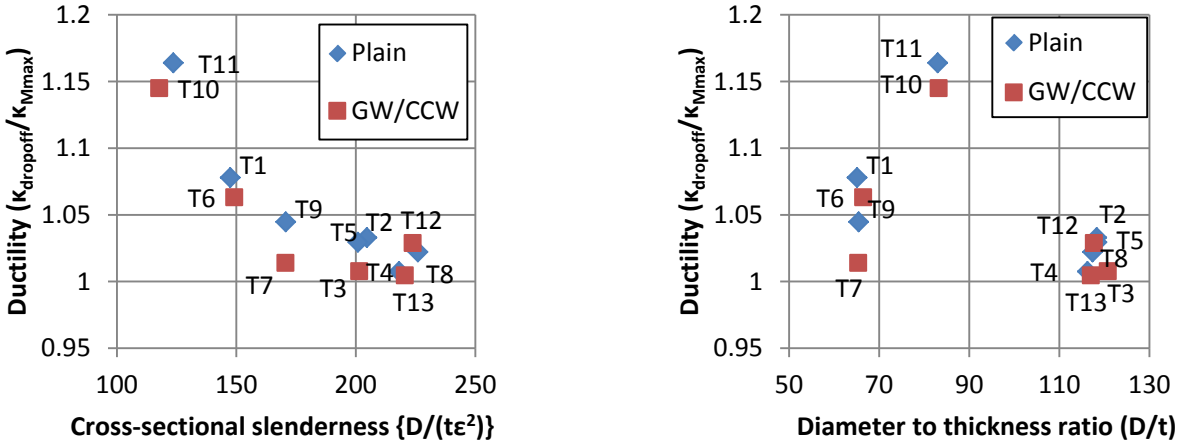


(a) Ductility with respect to slenderness parameter $D/(t\varepsilon^2)$

(b) Ductility with respect to slenderness parameter $D/t$

**Figure 36**: Comparison of specimen ductility, defined as the ratio between average curvature at load drop-off and at maximum bending moment.

## 5.4 Buckling location

From each specimen, the initial geometric profile of the intrados is known. Therefore, the location of the buckle can be related to the initial geometry to examine whether initial geometrical imperfections have triggered local buckling.

The development of a buckle may be recognized in the measurements of the geometry of the compression side of the specimen during the test (see Figure 8). The compression side geometry before buckling and at the onset of buckling is presented for two specimens in Figure 37. Note that in both cases the buckle occurs at a geometric imperfection. The results plotted in Figure 37b are particularly interesting: buckling has occurred at an initial geometric imperfection, which is certainly caused by the cold-forming process, since it aligns with a roller mark. As discussed in section 4, all regular geometric imperfections are assumed to be caused by the cold-forming process. Since these imperfections are apparently leading in forming a weak link in the tube, the cold-forming manufacturing process may have a direct influence on the local buckling behavior of these tubes.

It is worth noticing that in all but one specimen, local buckling has occurred away from the spiral weld, although in many cases, significant imperfections are visible in that region. Apparently the

influence of other factors may result in the formation of a local buckle away from the weld. A stiffening effect from the overmatched weld material may constitute such a factor.

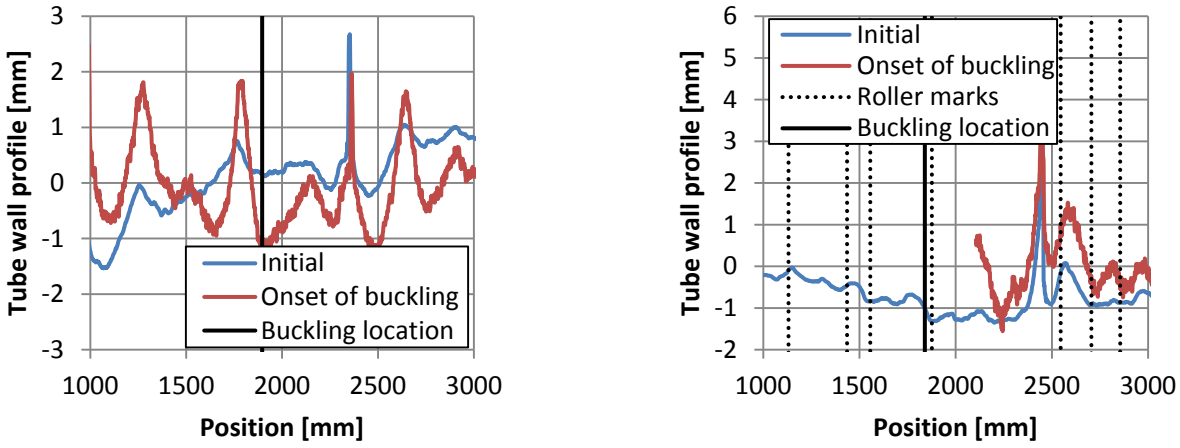


(a) Specimen T4 (b) Specimen T1

**Figure 37**: Buckling location for specimens T4 and T1. Monitoring of compression side during test T1 was only performed over part of the tube. Buckling occurred outside these measurements.

In case of specimens containing a girth weld or coil connection weld, the geometrical imperfections near that weld are generally larger than the imperfections in the plain tube specimens (compare Table 3 and Table 4). Considering that in plain tubes the geometrical imperfections cause a "weak link", it is expected that in case of these welds with larger geometrical imperfections, local buckling occurs at the weld area. In four out of the six specimens with these welds, local buckling occurred in the vicinity of weld. In the other cases, local buckling occurred away from those welds. Possible causes for this are discussed in section 5.5

### 5.5 Influence of the presence of girth welds and coil connection welds.

The presence of girth welds and coil connection welds may have a severe influence on the bending behavior of the tube. Firstly, these weld acts as a boundary between two specimen parts which may have different cross-sectional properties. Secondly, the weld may be associated with severe geometrical imperfections. Finally, the welding itself has influences due to heat input and added material.

Even in the case of a connection between two tubes that are identical by specification, the diameter, wall thickness and especially material behavior will differ to some extent. This implies a strong and a weak side of the weld. In this analysis, the product of wall thickness and yield strength is used as measure of strength of either side. In the experiments, all four local buckles that formed at a girth weld or coil connection weld, occurred at the weaker side. In specimen T12, where local buckling occurred away from the weld, local buckling occurred in the weaker side. In the other specimen where local buckling took place away from the weld (T7), local buckling occurred not in the weaker part. However,

differences in strength are limited to about 1% between the three specimen parts of this specimen, meaning that, for this specimen, effectively there is no "weak link" in terms of cross-sectional properties. A second implication of the difference in bending resistance between two sides of the weld is that curvature concentrates on the weaker side of the weld. This is an unfavorable situation, since this weaker section has a lower resistance against local buckling. In the experiments, the localization of curvature is clearly visible in the results of specimen T10 (see Figure 38a).

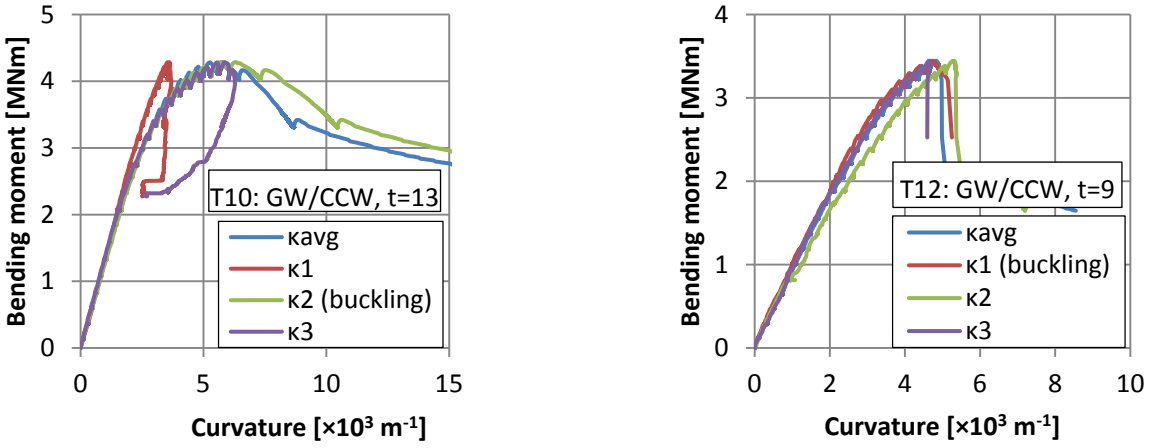


(a) Specimen T10 (b) Specimen T12

**Figure 38**: Effects of girth welds and coil connection welds on moment-curvature behavior.

The geometrical imperfections that are created by the girth welds and coil connection welds can be in the form of misalignments or geometrical imperfections of similar shape as the "hills" and "valleys" observed in plain tube sections. As shown in section 3.2, these initial imperfections near the welds are significant, and since many of the local buckles occur at this location, they may have a negative effect on buckling resistance. These imperfections might locally lead to a slightly higher curvature of the tube. Experimental observations show that very locally, the tube undergoes a rotation around the hinge that is formed by the imperfection. This effect is visible in Figure 38b, where the curvature over the girth weld ($\kappa_2$) is significantly higher than the other curvature measurements during almost the full test.

Welding itself has two implications. Firstly, welds feature a thicker material with higher yield strength (overmatched welds), thus the weld has a stiffening effect that might increase the local buckling resistance. Since many local buckles occurred at these welds and many specimens featuring such a weld exhibit lower local buckling resistance, this effect is deemed to be minor compared to other effects such as the aforementioned effects due to differences in cross-sectional properties and geometrical imperfections. Secondly, all welding results in residual stresses. These residual stresses may have an influence on local bucking.

As mentioned in section 5.4, two out of the six specimens including a girth weld or coil connection weld failed in local buckling away from the weld. In specimen T7, the misalignment and other geometrical imperfections measured at the girth weld are not so severe. Furthermore, due to its stockiness specimen T7 is less sensitive to geometrical imperfections, which allows other factors to be

decisive in the formation of a local buckle. In specimen T12, local buckling also took place away from the welds. The geometrical imperfections at the girth weld were indeed relatively small, but the initial geometrical imperfection at the coil connection weld was quite large. The specimen consisted of three parts, where the middle part had both a larger yield strength (by 13%) and thickness (by 2%), both significantly increasing its strength. As a result, this stronger part might have been able to support the attached weaker parts close to their welded connection. This support may prevent the formation of a buckle, as well as reduction of cross-sectional ovalisation. Further away from the welds (GW and CCW), the plain, weaker specimen parts apparently were more vulnerable to buckle. It must be noted that the aforementioned "support effect" could also be expected to prevent local buckling at the girth weld in specimen T10, where an even larger difference in strength between the adjacent parts exists. In that case however, local buckling took place at the girth weld, very likely triggered by the very large initial geometrical imperfection at that location (see Table 4)

Overall, it can be concluded that the critical curvature (deformation capacity) of specimens containing a girth weld or coil connection weld is generally lower (see Figure 34). The maximum resisted bending moment is equal to or lower than similar plain specimens (see Figure 33). Curvature seems to localize more than for plain specimens (see Figure 35), especially so for specimens where buckling occurred at the weld (T3, T6, T10, T13).

Because of this difference in curvature localization, a comparison of critical strains based on local curvature instead of average curvature (as in Figure 34) results in less discrepancy between plain specimens and specimens containing a girth weld or coil connection weld. However, even when the local curvatures are used, tubes containing a girth or coil connection weld are on the lower end of the scatter band in terms of their strength and deformation capacity.

Finally, the difference between reaching the maximum bending moment and load drop-off due to local buckling (ductility) is lower in specimens that contain such a weld (see Figure 36).

## 6 CONCLUSIONS

This paper presents a summary of the results obtained from thirteen full-scale four-point bending tests on 42-inch-diameter spiral-welded steel tubes. Initial geometry, wall thickness, diameter have been carefully documented before testing. Furthermore, an extensive study into the material properties of the tubular specimens has been performed.

In the bending tests, curvature localizes before the maximum bending moment is reached due to variations in bending moment capacity over the length of the specimen and is not uniformly distributed over the area with constant bending moment. This may have consequences for the prediction of deformation capacity in deformation-controlled loading cases in practice, since the assumption of equal curvature over a certain length with constant moment may no longer be valid.

The presence of girth welds and coil connection welds has shown to have a negative influence on tube resistance against local buckling. Furthermore, differences in terms of wall thickness and yield strength at such welds may trigger curvature localization; the weaker part of a tube will undergo more curvature, leading to local buckling.

The initial imperfections measured in the spiral-welded tubes appear to be the direct result of the production process. Buckles that occurred away from a girth weld or coil connection weld, developed at a geometrical imperfection caused by the cold-forming manufacturing process, showing the influence of the tube manufacturing process on the local buckling behavior.

An extensive investigation of various geometrical and material parameters using advanced finite element modelling is reported in the companion paper [30].

## ACKNOWLEDGMENTS

Funding for this work has been provided by the Research Fund for Coal and Steel (RFCS) of the European Commission, project COMBITUBE: "Bending Resistance of Steel Tubes in CombiWalls", Grant Agreement No. RFSR-CT-2011-00034.

## REFERENCES

[1] ArcelorMittal, 2010. "Spirally welded steel pipes", Advertisement Publication

[2] ArcelorMittal, 2008. "Cuxhaven – Greener Energy – thanks to ArcelorMittal sheet piles" [Online] Available: http://sheetpiling.arcelormittal.com/projects/display/title/cuxhaven. [Accesses 02-06-2015]

[3] Van Es, S.H.J., Gresnigt, A.M., Kolstein, M.H., Bijlaard, F.S.K., 2013. "Local buckling of Spirally Welded Tubes – Analysis of Imperfections and Physical Testing. *Proceedings of the International Offshore and Polar Engineering Conference (ISOPE),* Anchorage, USA.

[4] Gresnigt, A.M., Jo, C.H., Karamanos, S.A., 2011. "Local buckling of tubular sections in structural applications", *Proceedings of the 2011 World Congress on Advances in Structural Engineering and Mechanics (ASEM)*, Seoul, Korea

[5] Brazier, L.G., 1927. "On the Flexure of Thin Cylindrical Shells and Other Thin Sections", *Proceedings of the Royal Society, series A*, vol. 116, pp. 104-114.

[6] Moore, R.L., Clark, J.W., 1952. "Torsion, compression and bending tests of tubular sections machined from 75S-T6 rolled round rod", National advisory committee for aeronautics, Washington USA.

[7] Wilhoit, J.C., Merwin, J.E., 1973. "Critical Plastic Buckling Parameters for Tubing in Bending Under Axial Tension", *Proceedings of the Offshore Technology Conference,* Dallas, USA.

[8] Johns, T.G., Mesloh, R.E.W.R., Sorenson, J.E., 1975. "Inelastic Buckling of Pipelines under Combined Loads", *Proceedings of the Offshore Technology Conference,* Dallas, USA.

[9] Tugcu, P., Schroeder, J., 1979. "Plastic deformation and stability of pipes exposed to external couples", *International Journal of Solids and Structures*, vol. 15, pp. 643-658.

[10] Reddy, B.D., 1979. "An experimental study of the plastic buckling of circular cylinders in pure bending", *International Journal of Solids and Structures*, vol. 15, pp. 669-683.

[11] Van Douwen, A.A., Gresnigt, A.M., Stark, J.W.B., 1974. "Plastic design of buried steel pipelines for transport of oil, gas or water, verified by tests on scale models", TNO-IBBC, Rijswijk, The Netherlands.

[12] Kyriakides, S., Shaw, P.K., 1987. "Inelastic Buckling of Tubes Under Cycling Bending", *Journal of Pressure Vessel Technology*, vol. 109, pp 169-178.

[13] Kyriakides, S., Ju, G.T., 1992. "Bifurcation and localization instabilities in cylindrical shells under bending – Part I: Experiments", *International Journal of Solids and Structures*, vol. 29, no. 9, pp. 1117-1142.

[14] Ju, G.T., Kyriakides, S., 1992. "Bifurcation and localization instabilities in cylindrical shells under bending – Part II: Predictions", *International Journal of Solids and Structures*, vol. 29, no. 9, pp 1143-1171.

[15] Jirsa, J.O., Fook-Hoy, L., Wilhoit, J.C., Merwin, J.E., Rice, U., 1972. "Ovaling of Pipelines Under Pure Bending", *Proceedings of the Offshore Technology Conference*, Dallas, USA.

[16] Ades, C.S., 1957. "Bending Strength of Tubing in the Plastic Range", *Journal of Aeronautical Sciences,* pp. 605-610.

[17] Sherman, D.R., 1976. "Tests of circular steel tubes in bending", *Journal of the Structural Division of ASCE*, vol. 102, no. ST11, pp. 2181-2195.

[18] Dorey, A.B., Murray, D.W., Cheng, J.J.R., 2000. "An experimental evaluation of critical buckling strain criteria", *Proceedings of the International Pipeline Conference*, Calgary, Canada.

[19] DelCol, P.R., Grondin, G.Y., Cheng, R.J.J., Murray, D.W., 1998. "Behaviour of Large Diameter Line Pipe Under Combined Loads, Structural Engineering Report No. 224. University of Alberta, Department of Civil and Environmental Engineering, Alberta, Canada.

[20] Dorey, A.B., Murray, D.W., Cheng, R.J.J., Grondin, G.Y., 1999. "Testing and experimental results for NPS30 line pipe under combined loads", *Proceedings of the International Conference on Offshore Mechanics and Arctic Engineering (OMAE)*, St. Johns, Canada.

[21] Mohareb, M.E., Elwi, A.E., Kulak, G.L., Murray, D.W., 1994. "Deformation Behaviour of Line Pipe, Structural Engineering Report No. 202", University of Alberta, Department of Civil Engineering, Alberta, Canada.

[22] Yoosef-Ghodsi, N., Kulak, G., Murray, D.W., 1994. "Behaviour of Girth-Welded Line Pipe, Structural Engineering Report No. 203", University of Alberta, Department of Civil Engineering, Alberta, Canada.

[23] Bouwkamp. J.G., 1975. "Buckling and Post-Buckling Strength of Circula Tubular Sections", *Proceedings of the Offshore Technology Conference*, Dallas, Texas.

[24] Bouwkamp, J.G., Stephen, R.M., 1974. "Full-scale studies on the structural behaviour of large diameter pipes under combined loading", Structural Engineering Laboratory, University of California, Berkeley.

[25] Van Foeken, R.J., Gresnigt A.M., 1998. "Buckling and Collapse of UOE manufactured steel pipes – PR-238-9423", TNO, Rijswijk, The Netherlands.

[26] Gresnigt, A.M., Van Foeken, R.J., 2001. "Local Buckling of UOE and Seamless Steel Pipes", *Proceedings of the International Offshore and Polar Engineering Conference (ISOPE),* Stavanger, Norway.

[27] Zimmerman, T., Xie, J., Timms, C., Asante, J., 2004. "Buckling resistance of large diameter spiral welded linepipe", *Proceedings of the International Pipeline Conference (IPC)*, Calgary, Canada.

[28] Zimmermann, S., Karbasian, H., Knoop, F.M., 2013. "Helical Submerged Arc Welded Line Pipe Engineered For Strain Based Design", *Proceedings of the International Offshore and Polar Engineering Conference (ISOPE)*, Alaska, USA.

[29] Combitube Research Group, 2015. "Bending resistance of steel tubes in CombiWalls – COMBITUBE – Final Report, European Commission – Research Programme of the Research Fund for Coal and Steel, Brussels, Belgium.

[30] Vasilikis, D., Karamanos, S.A., Van Es, S.H.J., Gresnigt, A.M., 2015. "Ultimate Bending Capacity of Spiral-Welded Steel Tubes – Part II: Predictions", *International Journal of Mechanical Sciences*, submitted for review.

[31] Det Norske Veritas, 2010. "Offshore Standard OS-F101 – Submarine Pipeline Systems", DNV, Oslo, Norway.

[32] Sadowski, A.J., van Es, S.H.J., Reinke, T., Rotter, J.M., Gresnigt A.M., Ummenhofer, T., 2015. "Harmonic analysis of measured initial geometric imperfections in thick spiral-welded steel Combitubes", *Engineering Structures*, vol. 85, pp. 234-248.

[33] Timoshenko, S.P., Gere, J.M., 1961. "Theory of Elastic Stability", Dover Publications, New York, USA.

[34] American Institute of Steel Construction, 2010. "Specification for Structural Steel Buildings, AISC, Chicago, USA.

[35] European Committee for Standardization, 2006. "Eurocode 3: Design of steel structures - Part 1 - 1: General rules for buildings", CEN, Brussels, Belgium.